Computer Control of Tokamak Plasma Equilibrium

トカマク型核融合装置における
平衡プラズマの計算機制御に関する研究

栗原研一

Computer Control of Tokamak Plasma Equilibrium

KENICHI KURIHARA

November 1992

トカマク型核融合装置に於ける
平衡プラズマの計算機制御に関する研究

1992年 11月

栗原　研一

トカマク型核融合装置に於けるプラズマの平衡制御に関する問題（プラズマ位置形状の同定、位置形状の実時間制御モデル、プラズマ·コイル·構造物の電磁気的相互作用解析）を応用電磁気学を中心とする数理物理学の観点で検討し、デジタル計算機を用いた平衡トカマク·プラズマの実時間制御系（ハードウェア及びソフトウェア）の構築方法を扱った研究。

連絡先：　栗原研一
日本原子力研究所　那珂研究所　核融合装置試験部　JT-60第1試験室
〒311-01 茨城県那珂郡那珂町大字向山801-1
Telephone：0292-70-7423 (Office), 0292-82-8275 (Home), Facsimile：0292-70-7459 (Office)

Computer Control of Tokamak Plasma Equilibrium

Contents

トカマク型核融合装置に於ける平衡プラズマの計算機制御に関する研究

目　　次

Preface

"*Controlled Thermonuclear Fusion Energy*" has been for long expected to release human beings from anxiety about lack of energy. It is because it has desirable features that its fuel, deuterium, exists inexhaustibly in seawater, no activated waste is produced, etc. Several approaches have been advanced to date, but they seem to still leave a long distance to the goal. One of the most difficult problems in controlled fusion research is the complete understanding of plasma behavior, in spite that the theoretical and experimental investigation has been eagerly conducted.

Of these controlled fusion experimental devices, "tokamaks" have made the most promising results toward a "break-even" condition, since the first introduction in the middle of 1950s. To study plasma behavior in a tokamak, many devices have been developed in the world and some of them are in operation.

In the tokamak experiment, fortunately, it is not so difficult to produce and maintain a pulse of plasma discharge to a certain extent by a simple trial-and-error method. Then it has been emphasized to improve the plasma performance indices such as energy/particle confinement time, ion temperature and density in the hope of realizing controlled nuclear fusion. These indices result from the microscopic interactions of particles with electromagnetic fields. The external macroscopic electromagnetic fields are artificially controlled by the actuators such as poloidal/toroidal field coils. Therefore, manipulation of macroscopic quantities performs more important a task than that to maintain a plasma. In fact, it is known that high confinement mode (H-mode) and locked-mode disruptions are sensitive to the clearance from the wall and plasma current evolution, respectively, both of which can be controlled by the electromagnetic field applied to the plasma. They seem to show the significance of looking from a macroscopic stand point.

A way of looking at a plasma macroscopically is an "equilibrium control analysis," where a plasma is supposed to preserve its external/internal force balance like a conductor whose position, shape and current profile (conductivity) are evolving during a pulse of discharge. This simplification is valid in the time scale of macroscopic manipulation, ~1 msec, which is sufficiently longer than the time scale that an acceleration of a plasma is

settling to zero, ~1 μsec. (Analysis of conductivity evolution would require "transport analysis" to be involved.) Consequently, the design and operation of plasma control for a tokamak experimental device is based on the equilibrium control analysis.

In addition, to realize the design and operation of plasma control system, the utilized hardware performance is the other important element. The recent rapid advance of digital computer technology allows us to apply various kinds of complicated algorithms to plasma control. This enables the fast and accurate control of plasma equilibrium with high reliability and reproducibility.

The objective of this thesis is to investigate how to design and operate plasma equilibrium control with digital computers. Problems in control of tokamak plasma equilibrium — plasma shape identification, coil-vessel-plasma electromagnetic interactions, plasma control dynamics model, etc. — are discussed from the view points of applied mathematics and electromagnetics. It is presented how the JT-60 and JT-60U plasma real-time control system were designed and constructed using digital computers. A synthesis of tokamak plasma equilibrium control is finally proposed.

Kenichi Kurihara

Correspondence to Kenichi KURIHARA: JT-60 Facility Office I, Department of Fusion Facility, Naka Fusion Research Establishment, Japan Atomic Energy Research Institute, 801-1 Mukoyama Naka-machi Naka-gun Ibaraki-ken, 311-01, JAPAN. Facsimile: +81- 292(70)7459

Chapter I

Introduction

I.1 Concept of Tokamak Plasma Equilibrium Control

Controllability of tokamak plasma properties is a basic but unsolved problem. The difficulties are as follows:

(1) All the relations of the many distributed state quantities and the small number of actuators have not yet been made clear. The distributed state quantities are the profiles of plasma current, temperature and density, position and shape of a plasma column, electromagnetic fields and energy/particle confinement (flow). These are not independent, but interact each other. On the contrary, the major actuators are the several poloidal field coils, toroidal field coil, gas fueling, NBI (neutral beam injectors), RF (radio frequency heating devices), pellet injectors.

(2) The condition of the first wall facing a plasma is uncontrollable and usually unobservable. The activation extent of the wall determines the particle recycling ratio, which is known to be very sensitive to the edge plasma properties affecting the macroscopic plasma performances.

All the difficulties must be solved in the future as a result of various investigations with experiments. To perform the experiments, a plasma should be produced and maintained properly at first. Then this makes it possible to study other properties. The important parameters concerning production and maintenance of a plasma are its positions and shape. In the time scale of plasma position and shape control, a plasma can be regarded to preserve its external and internal force balance like a conductor. Consequently, in order to obtain a desired equilibrium plasma, it is necessary to control the plasma.

The configuration of the plasma equilibrium control in a tokamak is now shown in Fig. 1[*]. Four processes are linked through data or physical quantities: (a) "Identification" is to identify plasma configuration parameters, position and shape, from measured signals. (b) "Control algorithm" is to perform control calculations by comparing the identified parameters with preset reference waveforms according to a certain algorithm. It produces control commands to actuators. The control algorithm depends on the

[*] ; Control of plasma electron density is performed in the same way as shown in Fig. 1. Some actuators such as NBI and RF are operated according to preset waveforms without feedback control.

performance index and status of a plasma. Various algorithms are proposed for optimal plasma control. (c) "Actuators' dynamics" is composed of power supplies and poloidal field (PF) coils to produce electromagnetic fields according to the received commands. This process cannot be completely separated from that in "plasma & structural components." (d) "Plasma & structural components" interact with each other and with electromagnetic fields. Eddy currents induced in the structural conductors also interact PF coils, which is shown as the returning flow to "actuators' dynamics" in Fig. 1. As a result of those interactions, plasma position, shape and moving velocity are determined.

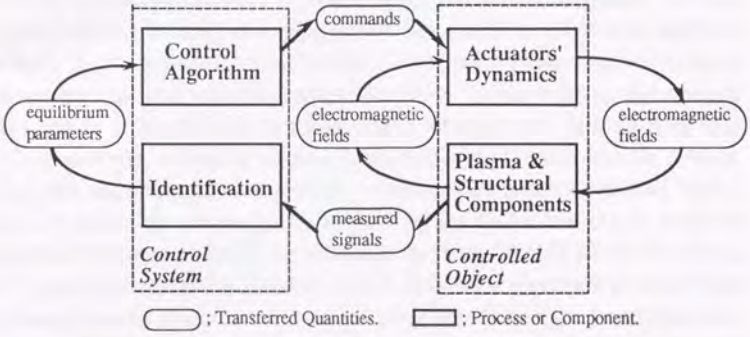

Fig. 1. Configuration of Tokamak Plasma Equilibrium Control

I.2 Objectives of This Thesis

The objectives of this thesis are now clarified together with the previous works in this field, .

Concerning tokamak plasma shape identification, many methods have been proposed[1], but few of them seem to have a rigorous mathematical basis. For example, filament-coil-plasma approximation[2], which is the most popular method for the full shape identification, has not been verified mathematically. Furthermore, rational determination of both the utilized sensors and their locations for the design of a new device does not exist. Thus, it is necessary to solve a shape identification problem on the basis of applied mathematics.

The shape identification can be regarded a kind of a static problem if the current distribution is determined. On the other hand, such an equilibrium plasma has "dynamics" because it moves electromagnetically interacting with the vacuum vessel, poloidal field coils, support structures, etc., where induced eddy currents produce electromagnetic field dynamics. Various kinds of eddy

current analyses are performed for electromagnetic industrial products in the world[3]. In addition, the benchmark tests to evaluate numerical codes for eddy current analyses were reported[4]. However, only a few numerical analyses have been applied to tokamak plasma equilibrium control[5]. Though those methods adopt various approximations of a tokamak device, they seem never to have been verified in the experiments. A simple model of plasma equilibrium control must be first constructed using Maxwell equations. Second, the model should be verified in comparison with experimental data from the JT-60 tokamak. Finally, a finite element method of plasma equilibrium control analyses is developed for three-dimensional general tokamak geometry.

Once a model for plasma equilibrium control is completed, various control methods can be applied to the model. The obtained preferable methods will be built in the plasma control system. However, at this stage of seeking experimentally the best tokamak operation for a fusion reactor, the control methods must be changed whenever a new understanding of plasma behavior is added. Consequently, a flexible system is required for tokamak plasma control. To realize the requirement, it seems to be natural to adopt advanced digital computers, because they have good reproducibility and reliability in addition to flexibility. No large tokamak device early in 1980s except JT-60, however, adopted digital computers for plasma control. It is then important to show how JT-60 plasma control system using digital computers is designed and operated. Furthermore, JT-60 Upgrade plasma control system, which allows any control method to be quickly and easily installed, provides one of the sophisticated systems for tokamak plasma equilibrium control with digital computers.

Now the objectives of this thesis are listed up as follows:

(1) To develop a new method to identify tokamak plasma shapes by solving a partial differential equation governing the problem of concern on the basis of applied mathematics. The method must give criteria to determine rationally both the utilized sensors and their locations.

(2) To construct a simple model of plasma equilibrium control using basic electromagnetic equations (e.g. Maxwell equation, Ohm's law, etc.). The model should be verified in comparison with experimental data from the JT-60 tokamak. A finite element method of plasma equilibrium control analyses is formulated for three-dimensional general tokamak geometry.

(3) To present how the plasma control systems for JT-60 and JT-60 Upgrade are designed and operated, as the sophisticated examples of tokamak plasma equilibrium control systems with digital computers.

(4) Finally, this thesis is intended to clarify synthetically how to build up "computer control of tokamak plasma equilibrium" from a methodological point of view. As this thesis contains all components necessary for plasma equilibrium control, it is believed to be of great use for the improvements or new developments of a tokamak system.

The abstracts of the chapters are presented as follows: In Chapter II, two methods of tokamak plasma shape identification are developed and discussed from an applied mathematical point of view. A necessary condition for shape identification is derived and application to JT-60 Upgrade and ITER (International Thermonuclear Experimental Reactor) plasmas are presented.

In Chapter III, electromagnetic interactions in a tokamak are investigated. Modelling of the controlled object dynamics is discussed and the validity is confirmed using JT-60 experimental data. Furthermore, electromagnetic equations for plasma equilibrium dynamics are derived, where axisymmetric motion is considered with the inputs of PF coil voltages and plasma pressure profile. A three-dimensional finite element method of plasma equilibrium control analyses is formulated for the tokamak geometry.

In Chapter IV, design and operation of JT-60 and JT-60 Upgrade plasma control systems using digital computers are presented from the technological aspects of software and hardware. In particular, how to build up a parallel and pipeline computer system is presented. System design of real-time shape visualization is also presented.

In Chapter V, conclusions derived from the investigations in the previous chapters are presented. A synthesis to design a tokamak plasma equilibrium control system is finally proposed as a result of the discussions in this thesis.

References in Chapter I.2

[1] Braams, B.J., Plasma Physics and Controlled Fusion, Vol.33 (1991) p.715.

[2] Swain, D.W., Neilson, G.H., Nuclear Fusion, Vol.22 (1982) p.1015.

[3] Many examples of eddy current numerical analyses are presented in "IEEE Transactions on Magnetics, Vol. Mag-23 (1987) No.5 and Vol. 26 (1990) No.5"

[4] Miya, K. and Nakata, T. (ed.), "Proceedings of the international workshop for eddy current code comparison," (Oct. 1986)

[5] Jardin, S.C. et al., "Dynamic modeling of transport and positional control of tokamaks," Journal of computational physics, Vol.66 (1986) p.481

Chapter II

Shape Identification of Tokamak Equilibrium Plasmas

As shape identification is indispensable for tokamak plasma experiments, many identification methods have been proposed. The methods for the real-time control are as follows:

(a) Shafranov moment method [1]
(b) Multiple moment method [2]
(c) Flux extrapolation method [3]
(d) Statistical processing formulation using the equilibrium database [4]

These methods can well identify only the plasmas having certain shapes, positions and internal quantities. In particular, (a) and (b) can be used only for circular plasmas. It is because long computation time is not allowed in real-time processing. Does adequate calculation time make it possible to reproduce the complete shape of plasmas? The full-shape identification methods proposed to date are then as follows:

(e) Filament-current-plasma approximation method [5]
(f) Eigenfunction expansion of a vacuum poloidal flux function in cylindrical coordinates [6]
(g) Eigenfunction (Legendre-Fourier) expansion of a vacuum poloidal flux function in toroidal coordinates [7]
(h) Optimal control method with a Cauchy boundary condition [8]
(i) Green's function method [9]
(j) Full equilibrium analysis [10]

The method (e) requires many independent parameters such as positions of the filament currents to be identified, and no algorithm to determine the filament-current locations has been found. This method gives a comparatively good result, though it was heuristically introduced and is not based on the theoretical certification.

Both the methods (f) and (g) analytically solve the Grad-Shafranov equation in a vacuum region. The method (f) uses an expansion of regular functions, while the method (g) uses that of functions with a singular point at the expansion center. The analytic region of concern is a doughnut-shape

vacuum are surrounding a plasma in a poloidal cross section. It is easily explained that a vacuum poloidal flux function in such a field that is not simply connected must have a singular point. Hence, the method (g) seems to be more preferable than the method (f). Furthermore, the method (g) can identifies both the shape of a small circular plasma and that of an asymmetric divertor plasma. This can also take eddy current into consideration.

The method (h) needs flux loop values. As flux values are obtained by the time-integral of the flux loop signals, and as the integrator must have the drift characteristics, this method is less suitable for steady-state tokamak operation. The necessity that the optimal control algorithm should be applied to this problem seems to be based on the Cauchy problem. But the reason why the Cauchy condition is necessary is unclear.

The method (i) also corresponds to solving the Grad-Shafranov equation in a vacuum region analytically. This method uses both the flux loop and probe signals. The flux loop signal is less suitable for steady-state discharge, similarly to the method (h).

The method (j) is to solve the Grad-Shafranov equation both in the vacuum and plasma regions under the assumption of the formulas of plasma current/pressure profiles. The necessity of the Grad-Shafranov equation in the plasma region is still questionable.

All the methods above still have problems in (steady-state) plasma operation, though analytical solutions of the Grad-Shafranov equation in a vacuum (the methods (g) and (i)) seem to be the most promising methods. However, why do so many arguments on shape identification still remain after so many method was proposed? This question may be caused by the inadequate theoretical (mathematical) consideration. This chapter is devoted to the clarification of the problem from the analytical point of view, the derivation of a necessary condition for shape identification, and the confirmation with applications.

In Chapter II.1, A method to identify the shape of tokamak plasmas with a Legendre-Fourier expansion of the vacuum poloidal flux function in toroidal coordinates is improved for the JT-60 Upgrade plasmas that have different sizes, positions, shapes and internal quantities. The method is based on the analytical solution of the Grad-Shafranov equation in a vacuum region using toroidal coordinates. Though many identification methods proposed previously allow very small perturbations of certain parameters of nominal plasma, the method presented in this article can relax the identification restriction on plasmas. Hence, it is applicable to accurate feedback control and real-time

visualization of various plasma configurations. Both the method and the computational algorithm are clearly presented. A comparison of this method with the filament-current approximation method is described. Robustness in the case of the unavailability of sensors or with signal noise is also examined in application to the JT-60 Upgrade tokamak geometry.

In Chapter II.2, The mathematical concepts of necessary conditions for tokamak plasma shape identification are discussed. A method using only the derived necessary condition is proposed. This method is based on the boundary integral equations governing a vacuum region around a plasma with only the measurement of either magnetic fluxes or magnetic flux intensities. The application to JT-60U and ITER plasmas shows that this method can identify various plasmas with low to high ellipticities with the necessary precision by providing an adequate number of the magnetic sensors. The proposed method is also applicable to real-time control and visualization by utilizing tabulated "look-up" data.

References

[1] Mukhovatov, V. S. and Shafranov, V. D., "Plasma Equilibrium in a Tokamak," Nuclear Fusion vol.11(1971), p.605.

[2] Aikawa,H. et al., "Derivation of Plasma Displacement in a Tokamak from Magnetic Probe Signals," Japanese Journal Applied Physics vol.15(1976), p.2031 & p.2479.

[3] Schneider, F., "Novel Method of Determining the Plasma Position and its Application to the ASDEX Feedback System," Proceedings of 10th Symposium on Fusion Technology, Padova(1978), p.1013.

[4] Hosogane, N. et al., "Method for Measuring Divertor Configuration Parameters for Feedback Control in JT-60," Nuclear Fusion vol.26(1986), p.657.

[5] Swain,D.W. and Neilson,G.H., "An Efficient Technique for Magnetic Analysis of Non-circular, High-beta Tokamak Equilibria," Nuclear Fusion vol.22(1982), p.1015.

[6] Reusch,M.F. and Neilson,G.H., "Finite Order Polynomial Moment Solutions of the Homogeneous Grad-Shafranov Equation," Princeton Plasma Physics Laboratory Report PPPL-2072(1984).

[7] Lee,D.K. and Peng,Y.-K.M., "An Approach to Rapid Plasma Shape Diagnostics in Tokamaks," Journal of Plasma Physics vol.25 (1981), p.161.
Alladio,F. and Crisanti,F., "Analysis of MHD Equilibria by Toroidal Multipolar Expansions," Nuclear Fusion vol.26(1986), p.1143

[8] Blum,J., "Numerical Simulation and Optimal Control in Plasma Physics with Application to Tokamaks," John Wiley and Sons (1988).

[9] Hakkarainen, S.P. Lecture Note on MHD and Related Topics in Alcator C-mod, at JAERI on Dec. 25 (1989)

[10] Luxon,J.L. and Brown,B.B., "Magnetic Analysis of Non-circular Cross-section Tokamaks," Nuclear Fusion vol.22(1982), p.813.

II.1 Tokamak Plasma Shape Identification with a Legendre-Fourier Expansion of the Vacuum Poloidal Flux Function

1. Introduction

Since the tokamak was first introduced in the middle 1950s, various methods for position and shape identification have been developed for plasma control and diagnosis[1]~[12]. These methods are roughly classified into two types; calculation of macroscopic parameters and full-shape identification. The former aims at real-time feedback control, where the calculation time is required to be minimized. The latter is required to identify full plasma shapes more accurately, even if a much longer calculation time is needed. Now we address the latter methods with a poloidal flux function expressed by a series of eigenfunctions of the Grad-Shafranov(G-S) equation in a vacuum region. These functions are used because they are well supported by the mathematical theory of the solution of partial differential equations.

The form of an eigenfunction depends on the coordinates taken for the analysis. Eigenfunctions in cylindrical, spherical and toroidal coordinates have been applied to tokamak devices. Eigenfunctions of the G-S equation in other coordinates can be mathematically considered, but other coordinates have not been used for tokamak plasma applications. Selection of the coordinates has a strong influence on the accuracy of approximation of the finite series of eigenfunctions. When the configuration of the coordinates has similarity to the actual plasma shape, the identification can be more precisely performed and needs only the first several orders of eigenfunctions. Consequently, toroidal coordinates were chosen as a starting point because they basically expresses the contour of a complex potential field produced by a pair of positive and negative charges.

The requirements for the shape identification of the JT-60 Upgrade (JT-60U) plasmas (noncircular lower-divertor plasmas) [13] are listed below.
Req.1: An algorithm that can identify the shape precisely in real time and in various plasmas; from a small circular limiter plasma to a large noncircular divertor plasma with various internal quantities such as li, βp, etc. Req.2: An algorithm that can visualize the shape in real time. This will improve operation efficiency. Req.3: Eddy currents should be taken into consideration.

The previously proposed methods which use eigenfunctions in cylindrical, spherical and toroidal coordinates do not satisfy Req. 1; even a small amount

of positional perturbation increases the identification error. However, the sophistication of these algorithms and their integration with computer technology could satisfy Req. 2.

As a result of investigation, it was determined that the improved method described in this chapter can satisfy all requirements. In the following sections, this method —"the toroidal-coordinates Legendre-Fourier expansion (TOLFEX) method"—is explained together with its application to the JT-60U plasmas.

2 Poloidal Flux Function in a Vacuum Region

2.1 Analytical Solution of the Grad-Shafranov Equation in a Vacuum Region and Its Physical Interpretation

Two quasi-steady-state Maxwell's equations in a vacuum region;

$$\text{rot } \mathbf{B} = \mathbf{0}, \tag{2.1}$$

$$\text{div } \mathbf{B} = \mathbf{0} \tag{2.2}$$

give the Grad-Shafranov equation under the assumption of axisymmetric geometry. ϕ is a poloidal flux function.

$$r^2 \mathrm{div}\left(\frac{\mathrm{grad}\phi}{r^2}\right) = \left\{ r\frac{\partial}{\partial r}\left(\frac{1}{r}\frac{\partial}{\partial r}\right) + \left(\frac{\partial}{\partial z}\right)^2 \right\}\phi = 0 \tag{2.3}$$

Now we change the variables from (r, z) in cylindrical coordinates to (a, θ) in toroidal coordinates according to the following relations;

$$\coth a = \frac{r^2+(z-Z_0)^2+R_0^2}{2\,r\,R_0}, \quad \cot\theta = \frac{r^2+(z-Z_0)^2-R_0^2}{2\,(z-Z_0)\,R_0}. \tag{2.4}$$

Then, the solution of Eq. (2.3) is given as a series of flux eigenfunctions $\xi^G{}_m(r,z,R_0,Z_0)$ using the method of variable separation[14]):

$$\xi^G_m(r,z,R_0,Z_0) = \frac{\sinh a}{\sqrt{\cosh a - \cos\theta}} \cdot f_m(a) \cdot g_m(\theta) \tag{2.5}$$

$$f_m(a) = \frac{d\Theta_{m-1/2}(x)}{dx} \;:\; x = \cosh a$$

$$\Theta_{m-1/2} = \begin{matrix} P_{m-1/2} \\ Q_{m-1/2} \end{matrix} \quad \begin{matrix} \text{;(m-1/2)-order Legendre function of the 1st kind} \\ \text{;(m-1/2)-order Legendre function of the 2nd kind} \end{matrix}$$

$$g_m(\theta) = \begin{matrix} \cos m\theta \\ \sin m\theta \end{matrix}$$

m = 0,1,2,.....; separation constants.

Each flux eigenfunction $\xi^G{}_m(r,z,R_0,Z_0)$ expresses a two-dimensional potential field produced by both currents of poloidal field coils and a plasma current. Flux eigenfunctions are classified into four types depending on the selection of the functions $f_m(a)$ and $g_m(\theta)$, as shown in Table 2.1. Figures 2.1 and 2.2 show

three-dimensional figures of flux eigenfunctions involving a Legendre function of the first and second kind, respectively.

Table 2.1 Classification of Flux Eigenfunctions

g_m \ $\Theta_{m-1/2}$	$P_{m-1/2}$	$Q_{m-1/2}$
cos mθ	P·cos	Q·cos
sin mθ	P·sin	Q·sin

Physical interpretation of the flux eigenfunctions is:

Pcos: m=0 : flux produced by a ring-filament current flowing through (R_0,Z_0).
=1 : flux produced by dipole currents.
=2 : flux produced by quadruple-pole currents.
=3~ : flux produced by (2m)-pole currents.

Psin: m=1~ : flux expressed by rotating the corresponding Pcos flux about (R_0,Z_0) by an angle of $\pi/(2m)$.

Qcos: m=0 : the 0-order of vertical magnetic field.
=1 : the 1st-order of vertical magnetic field.
=2 : magnetic field for changing ellipticity.
=3 : magnetic field for changing triangularity.
=4~ : magnetic field for an m-angle polygon.

Qsin: m=1 : horizontal magnetic field.
=2~ : flux expressed by rotating the corresponding Qcos flux about (R_0,Z_0) by an angle of $\pi/(2m)$.

In particular, a singular point in the flux eigenfunctions of Pcos and Psin is only a point of (R_0,Z_0), though higer order eigenfunctions can express the magnetic field produced by multipole currents. A series of flux eigenfunctions can express a figure of vacuum poloidal flux except the singular point (R_0,Z_0).

If a Dirichlet or a Neumann condition is given everywhere on a certain closed boundary, an infinite series of eigenfunctions could compose a solution of the G-S equation. Such an ideal supposition, however, can not be applied to an actual system. Hence, the flux functions produced by artificially-located poloidal field (PF) coils should be introduced for improvement of the identification.

The locations of PF coils are determined as a result of design of a tokamak plasma. A PF coil can be defined as several turns of ring currents, whose flux satisfies the G-S equation in a vacuum region. The PF coil flux function can be considered independent of the eigenfunction $\xi^G{}_m(r,z,R_0,Z_0)$ because there is only a small possibility that a flux function of an artificially-located PF coil agrees with a finite series of flux eigenfunctions introduced mathematically.

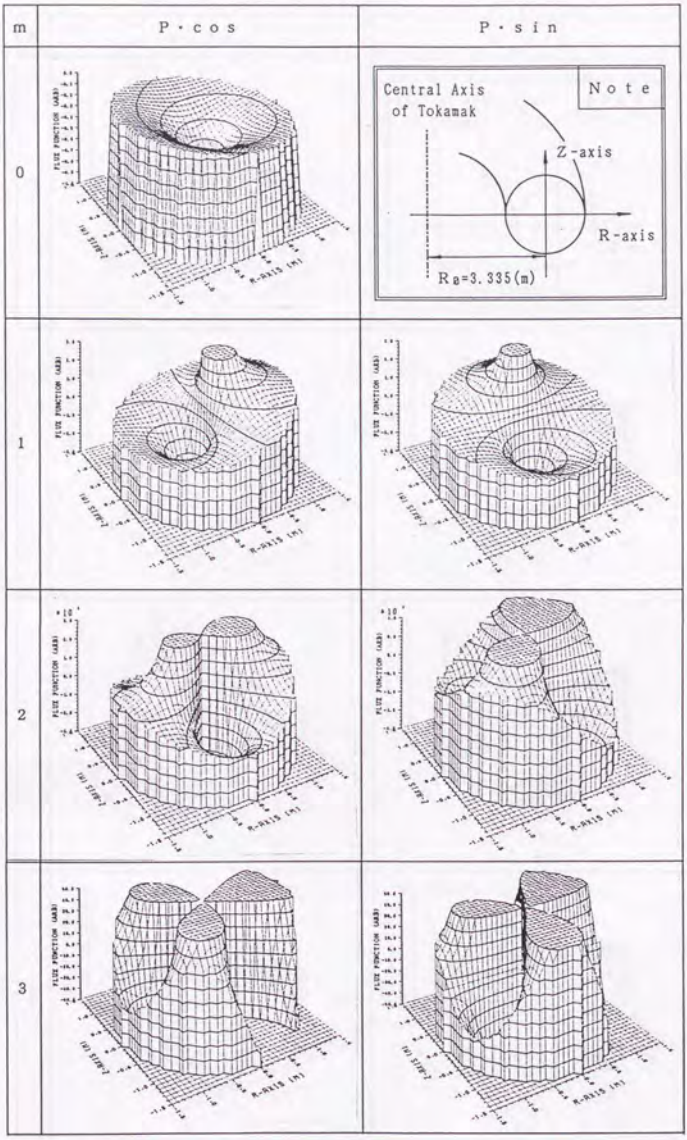

Fig. 2.1 Three Dimensional Figures of the Flux Eigenfunctions Containing a Legendre Function of the First Kind (m=0,1,2,3)

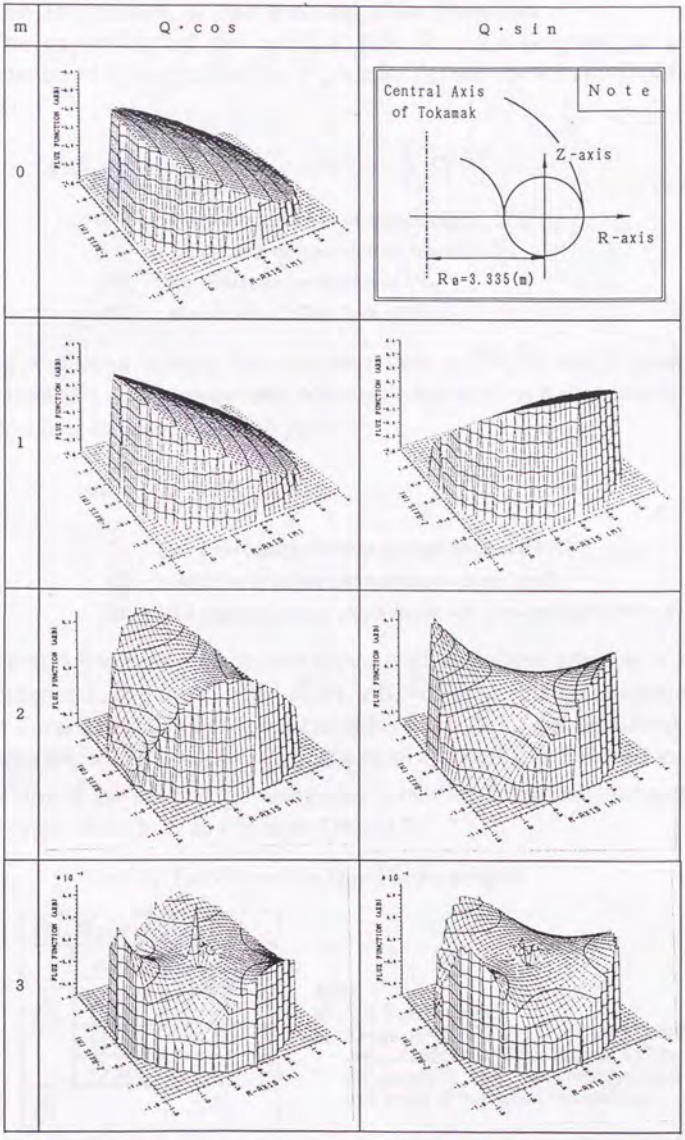

Fig. 2.2 Three Dimensional Figures of the Flux Eigenfunctions Containing a Legendre Function of the Second Kind (m=0,1,2,3)

2.2 The Expression of the Poloidal Flux Function

The expression of the poloidal flux function is given as a linear combination of the eigenfunction $\xi^G_m(r,z,R_0,Z_0)$ and the PF coil flux function $\xi^C_i(r,z)$.

$$\phi(r,z,R_0,Z_0) = \sum_{m=0}^{\alpha} C^G_m \cdot \xi^G_m(r,z,R_0,Z_0) + \sum_{i=1}^{\beta} C^C_i \cdot \xi^C_i(r,z) \ . \tag{2.6}$$

α ; the number of types of eigenfunction ξ^G_m.
β ; the number of types of flux function ξ^C_i.
C^G_m ; the unknown coefficient of ξ^G_m.
C^C_i ; the unknown coefficient of ξ^C_i.

Taking a plasma current into consideration, a C^G_m is easily eliminated. Integration of a quasi-steady-state Maxwell's equation rot $\mathbf{B}=\mu_0\mathbf{j}$ over the entire surface where current is flowing gives

$$\mu_0 I = \int \text{rot } \mathbf{B}\cdot d\mathbf{S} = \oint \mathbf{B}\cdot d\mathbf{l}. \tag{2.7}$$

I ; the total current flowing through the surface S.
dS ; $=\mathbf{n}\,dS$, $\mathbf{n}$ is the normal vector to the surface S.
dl ; the direction vector along the closed curve around surface S.

In general, a magnetic flux density vector is given as derivatives of a poloidal flux function ξ, and then; $r\cdot Br=-\partial\xi/\partial z$, $r\cdot Bz=\partial\xi/\partial r$. Using these relations, the closed linear integrals (the right-hand side of Eq. (2.7)) are calculated for the functions ξ^G_m and ξ^C_i analytically. If a point of (R_0, Z_0) is included inside the closed line of the integral, the integrated values are determined independently of the route of the line, as shown in Table 2.2.

Table 2.2 The Values of the Closed Linear Integrals

Flux Function		$\oint \mathbf{B}\cdot d\mathbf{l}$
ξ^G_m	P·cos	$\frac{5}{\pi R_0\sqrt{2}}$ a)
	P·sin	0 b)
	Q·cos	0 b)
	Q·sin	0 b)
ξ^C_i		0

Note:
a) : See Reference [15].
b) : Q·cos, m=0, 1, 2 and Q·sin, m=1, 2 are regular functions. Their integral values are exactly 0. Others can be regarded 0 as a result of numerical calculations.

Thus, Eq. (2.7) results in the following relation.

$$\sum^{(P\cdot\cos)} C_m^G = \frac{\pi\sqrt{2}}{5} R_0 \cdot \mu_0 \cdot \eta \cdot I_p \equiv k(R_0) \cdot I_p \quad . \tag{2.8}$$

I_p ; plasma current.

$\sum^{(P\cdot\cos)}$; summation of the coefficients of the eigenfunctions of P·cos.

η ; parameter for adjusting the coefficient of P·cos (η <1.0).

$k(R_0) \equiv \frac{\pi\sqrt{2}}{5} R_0 \cdot \mu_0 \cdot \eta$.

C^G_0 denotes the coefficient of the eigenfunction Pcos,m=0; then Eq. (2.8) gives

$$C_0^G = k(R_0) \cdot I_p - \sum_{m\neq 0}^{(P\cdot\cos)} C_m^G \quad . \tag{2.9}$$

Eliminating C^G_0 in Eq. (2.6) by using Eq. (2.9),

$$\phi = k(R_0) \cdot I_p \cdot \xi_0^G + \sum_{m\neq 0}^{(P\cdot\cos)} C_m^G \cdot (\xi_m^G - \xi_0^G) + \overline{\sum^{(P\cdot\cos)}} C_m^G \cdot \xi_m^G + \sum_{i=1}^{\beta} C_i^C \cdot \xi_i^C . \tag{2.10}$$

ξ_0^G ; the eigenfunction P·cos, m=0

$\sum^{(P\cdot\cos)}_{m\neq 0}$; summation of the eigenfunctions of P·cos, excluding P·cos,m=0.

$\overline{\sum^{(P\cdot\cos)}}$; summation of all eigenfunctions except P·cos.

The vector expression is now introduced in Eq. (2.10). Then

$$\phi(r,z,R_0,Z_0) = p(r,z,R_0,Z_0) \cdot I_p + {}^t\mathbf{q}(r,z,R_0,Z_0) \cdot \mathbf{C}. \tag{2.11}$$

$$p(r,z,R_0,Z_0) \equiv k(R_0) \cdot \xi_0^G .$$

$${}^t\mathbf{q}(r,z,R_0,Z_0) \equiv (\xi_1^G - \xi_0^G,\ \xi_2^G - \xi_0^G, \cdots,\ \xi_j^G, \xi_{j+1}^G, \cdots, \xi_1^C, \xi_2^C, \cdots).$$

$${}^t\mathbf{C} \equiv (C_1^G - C_0^G,\ C_2^G - C_0^G, \cdots,\ C_j^G, C_{j+1}^G, \cdots, C_1^C, C_2^C, \cdots).$$

$\mathbf{q}, \mathbf{C} \in \mathbf{R}^{(\alpha+\beta-1)\times 1}$, $\quad {}^t\mathbf{q}$; transpose the vector $\mathbf{q}$.

$\boldsymbol{C}$ and (R_0, Z_0) are identified from the signals of flux loops and a Rogowski coil. The necessary conditions for the existence of $\boldsymbol{C}$ and (R_0, Z_0) are easily obtained as

$$\alpha + \beta + 2(R_0, Z_0 \text{ search}) \leq (\text{number of flux loops}) + 1(\text{a Rogowski coil}). \tag{2.12}$$

Now this concept is discussed from a mathematical point of view. The G-S equation belongs to a second-order elliptic partial differential equation (PDE) that holds in the doughnut-shaped region surrounding a plasma surface. Figure 3 shows a topological concept of this region. A boundary condition is given only on the outermost boundary; the innermost boundary is free. Two

types of boundary conditions are possible; "Dirichlet" when flux loops are used and "Neumann" when magnetic probes are used. A Dirichlet type boundary condition is adopted for our method.

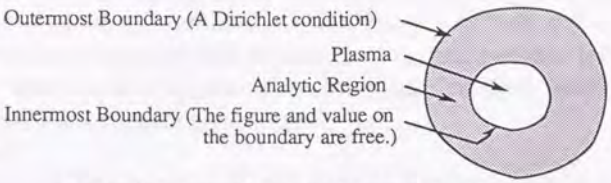

Fig. 2.3. Topological Concept of the Analytic Region

According to Morse and Feshbach[14], solutions of the second-order elliptic PDEs provides stable and unique results for Dirichlet conditions on a closed boundary. Consequently, the Dirichlet condition only on the closed outermost boundary (i.e., on the vacuum vessel wall) determines a unique solution over the concerned region including the innermost boundary (i.e., the plasma surface). Though the solution has been obtained on the entire doughnut-shaped region, information on the innermost boundary is never derived from consideration of differential equations. Instead, it is obtained from a tokamak plasma property. The outermost magnetic surface of a plasma is known to be defined by the contour with the same flux value. Therefore, once a flux value is given at a certain point on the innermost boundary, a contour with the same flux value must show the plasma shape. In a limiter discharge, all flux values at fixed limiters located on the vessel wall are calculated using this solution. The smallest value (or the largest value; depending on the selection of positive or negative direction) indicates the flux value on the plasma surface. In a divertor discharge, flux values at both the fixed limiters and an X-point (a saddle point of the solved flux function) are calculated. The smallest value indicates the surface flux value. The discussion above concludes in principle that this method can find a plasma shape from flux loop signals without any information on plasma internal quantities. In reality, however, the Dirichlet condition is given on discrete points on the boundary and the solution of an infinite series of eigenfunctions cannot be given exactly. Application to the JT-60U, discussed in Section 4, shows this does not present a problem.

3. Algorithm for Shape Identification

3.1 Identification of (R_0,Z_0) and C

The first step of shape identification is to determine (R_0,Z_0), the center of

the toroidal coordinates. The next step is to determine the coefficient vector $\boldsymbol{C}$. If (R_0, Z_0) is not identified but fixed, the identifiable plasmas are extremely restricted because of a finite series of eigenfunctions and discrete boundary conditions. Now, returning to Eq. (2.11), $\boldsymbol{C}$ is linearly contained, while (R_0,Z_0) is nonlinearly contained. It was found that both a linear and a nonlinear unknown quantity can be calculated by "the two-step least squares method." This method applies the least square method twice with the performance index remaining unchanged.

[Definition]

The number of flux loops is N, and each of their positions in cylindrical coordinates is (r_i, z_i), i=1,2,..N. The following quantities are defined.

$$\phi_i \equiv \phi(r_i,z_i,R_0,Z_0), \qquad \mathbf{h} \equiv {}^t(\phi_1,\phi_2,\cdots,\phi_N) \in \mathbf{R}^{N\times 1}.$$
$$p_i \equiv p(r_i,z_i,R_0,Z_0), \qquad \mathbf{p} \equiv {}^t(p_1,p_2,\cdots,p_N) \in \mathbf{R}^{N\times 1}.$$
$$q_i \equiv q(r_i,z_i,R_0,Z_0), \qquad \mathbf{F} \equiv {}^t(q_1,q_2,\cdots,q_N) \in \mathbf{R}^{N\times(\alpha+\beta-1)}.$$

Making N sets of Eq. (2.11) on the points of (r_i, z_i), i=1,2,..,N, the following vector equation is obtained.

$$\mathbf{h} = \mathbf{p}\cdot I_p + \mathbf{F}\cdot\mathbf{C}. \tag{3.1}$$

ϕ^{obs}_i is the observed data of the i-th flux loop and the vector $\mathbf{h}^{obs}$ is defined as:

$$\mathbf{h}^{obs} \equiv {}^t(\phi_1^{obs},\phi_2^{obs},\cdots,\phi_N^{obs}) \in \mathbf{R}^{N\times 1}. \tag{3.2}$$

[The least squares method is used to obtain this form of $\boldsymbol{C}$]

The performance index is defined as follows;

$$J = {}^t(\mathbf{h}^{obs}-\mathbf{h})\cdot(\mathbf{h}^{obs}-\mathbf{h}). \tag{3.3}$$

$\partial J/\partial \boldsymbol{C}=0$ gives the form of the least squares solution of $\boldsymbol{C}^{cal}$.

$$\mathbf{C}^{cal} = ({}^t\mathbf{F}\cdot\mathbf{F})^{-1}\cdot{}^t\mathbf{F}\cdot(\mathbf{h}^{obs}-\mathbf{p}\cdot I_p). \tag{3.4}$$

$\boldsymbol{C}^{cal}$ is substituted into $\boldsymbol{C}$ in Eq. (3.1) and the calculated flux vector $\mathbf{h}^{cal}$ is given as a function of (R_0,Z_0).

$$\begin{aligned}\mathbf{h}^{cal} &= \mathbf{p}\cdot I_p + \mathbf{F}\cdot\mathbf{C}^{cal} \\ &= \{\mathbf{E} - \mathbf{F}\cdot({}^t\mathbf{F}\cdot\mathbf{F})^{-1}\cdot{}^t\mathbf{F}\}\cdot\mathbf{p}\cdot I_p + \mathbf{F}\cdot({}^t\mathbf{F}\cdot\mathbf{F})^{-1}\cdot{}^t\mathbf{F}\cdot\mathbf{h}^{obs}. \\ &\quad \mathbf{E} \quad ;\text{A unit matrix} \in \mathbf{R}^{N\times N}.\end{aligned} \tag{3.5}$$

[The least squares method is used to obtain the performance index for (R_0,Z_0)]

The performance index for (R_0, Z_0) is set to the form of Eq. (3.3);

$$J = {}^t(\mathbf{h}^{obs}-\mathbf{h}^{cal})\cdot(\mathbf{h}^{obs}-\mathbf{h}^{cal}). \tag{3.6}$$

The right-hand side of Eq. (3.5) is substituted for $\mathbf{h}^{cal}$ in Eq. (3.6), then

$$J = {}^t(\mathbf{h}^{obs}-\mathbf{p}\cdot I_p)\cdot\{\mathbf{E} - \mathbf{F}\cdot({}^t\mathbf{F}\cdot\mathbf{F})^{-1}\cdot{}^t\mathbf{F}\}\cdot(\mathbf{h}^{obs}-\mathbf{p}\cdot I_p) \tag{3.7}$$

$$= {}^t\mathbf{h}^{obs}\cdot\mathbf{U}\cdot\mathbf{h}^{obs} + \mathbf{V}\cdot\mathbf{h}^{obs}\cdot I_p + W\cdot I_p^2. \tag{3.8}$$

$$\mathbf{U}(R_0,Z_0) \equiv \mathbf{E} - \mathbf{F}\cdot({}^t\mathbf{F}\cdot\mathbf{F})^{-1}\cdot{}^t\mathbf{F} \qquad \in \mathbf{R}^{N\times N}.$$

$$\mathbf{V}(R_0,Z_0) \equiv -2\cdot{}^t\mathbf{p}\cdot\{\mathbf{E} - \mathbf{F}\cdot({}^t\mathbf{F}\cdot\mathbf{F})^{-1}\cdot{}^t\mathbf{F}\} \qquad \in \mathbf{R}^{1\times N}.$$
$$\mathbf{W}(R_0,Z_0) \equiv {}^t\mathbf{p}\cdot\{\mathbf{E} - \mathbf{F}\cdot({}^t\mathbf{F}\cdot\mathbf{F})^{-1}\cdot{}^t\mathbf{F}\}\cdot\mathbf{p} \qquad \in \mathbf{R}^{1\times 1}.$$

It should be noted that the dimensions of **U** and **V** are determined not by the number of eigenfunctions but by the number of flux loops. A nonlinear search process over the three-dimensional curved surface of (r,z,J(r,z)) is required for obtaining a point (R_0, Z_0) that minimizes the performance index of Eq. (3.8). Once (R_0, Z_0) is determined, Eq. (3.4) gives the parameter $\boldsymbol{C}^{cal}$.

3.2 Identification of the Poloidal Flux Function

The substitution of $\boldsymbol{C}^{cal}$ in Eq. (2.11) gives the poloidal flux function ϕ at an arbitrary point of (r, z) in a vacuum region;

$$\phi(r,z) = p(r,z)\cdot I_p + {}^t\mathbf{q}(r,z)\cdot\mathbf{C}^{cal} \qquad (3.9)$$
$$= {}^t\mathbf{a}(r,z)\cdot\mathbf{h}^{obs} + b(r,z)\cdot I_p. \qquad (3.10)$$
$$\mathbf{a}(r,z) \equiv {}^t\mathbf{h}(r,z)\cdot({}^t\mathbf{F}\cdot\mathbf{F})^{-1}\cdot{}^t\mathbf{F} \qquad \in \mathbf{R}^{N\times 1}.$$
$$b(r,z) \equiv p(r,z) - {}^t\mathbf{h}(r,z)\cdot({}^t\mathbf{F}\cdot\mathbf{F})^{-1}\cdot{}^t\mathbf{F}\cdot\mathbf{p} \qquad \in \mathbf{R}^{1\times 1}.$$

On the three-dimensional curved surface of $(r,z,\phi(r,z))$ in the vacuum region, the flux values at the fixed limiters are calculated. The X-point search is also performed on the same surface. Among calculated flux values at both the fixed limiters and an X-point, the smallest one indicates the plasma surface flux value ϕ_{min}. The contour of $\phi(r,z)$ with ϕ_{min} then shows the shape of the plasma.

4. Performance Evaluation: Application to JT-60 Upgrade

4.1 Evaluation of Precision

In this section, the plasma shapes identified by the proposed method — TOLFEX (toroidal-coordinates Legendre-Fourier expansion) method are compared with those calculated by a reliable equilibrium code in JT-60U geometry. Seven types of eigenfunctions are used for JT-60U as follows; (1)Pcos:m=0, (2)Pcos:m=2, (3)Qcos:m=0, (4)Qcos:m=1, (5)Qcos:m=2, (6)Qcos:m=3 and (7)Qsin:m=1. These indispensable eigenfunctions together with the four flux functions produced by the PF coils were found to identify various JT-60U plasmas having different positions, shapes and internal quantities.

The η-value in Eq. (2.8) is a constant, 0.96, for various JT-60U plasmas. This signifies that two eigenfunctions, Pcos,m=0&2, express 96% of the total plasma current and that the higher order eigenfunctions probably specifies the remainder of the plasma current.

The dashed line in Fig. 4.1(a) shows the identified shape of a 6 MA standard divertor plasma and that in Fig. 4.1(e) shows a 6 MA standard limiter plasma case. Both identified shapes agree with the contours calculated by the

equilibrium code. Figure 4.1(h) is a 1 MA small limiter plasma attached to the inside wall of the vessel. The identification error is observed on the outside surface and on the tokamak center axis. It seems that the number of flux loops located on the outside wall of the vessel may be very inadequate and the distance from the flux loops to the plasma surface is too great to give a precise identification. Figure 4.1(d) is the case of a smaller divertor plasma with a low poloidal β-value. Good agreement can be seen despite the excessive distance from the plasma to the upper flux loops.

Errors related to the change of plasma current profiles are next investigated. Figures 4.1(b) and 4.1(c) show the case of a peaked-profile plasma and that of a broad-profile plasma as compared with the plasma in Fig. 4.1(a). Though the effective distance from the flux loops and the plasma becomes greater in the peaked-profile case (b), the error is small. In contrast, the effective distance becomes smaller in the broad-profile case (c), but the identified surface is rather wider in comparison with the reference shape. Figures 4.1(f) and 4.1(g) show good results for limiter plasmas with different positions.

Table 4.1 compares the TOLFEX method and equilibrium code major radii(= 1/2{(inner surface)-(outer surface)}) and the vertical positions. Λ is calculated according the reference [16]. The precision of the X-point, the unit of mesh, in the equilibrium code is 4 cm.

Table 4.1 Comparison of the Major Radii and the Vertical Positions between the TOLFEX Method and the Equilibrium Code Outputs

Items		Case 1	Case 2	Case 3	Case 4	Case 5	Case 6	Case 7	Case 8
Divert./Limit.		D	D	D	D	L	L	L	L
Ip		6 MA	6 MA	6 MA	2 MA	6 MA	4 MA	2 MA	1 MA
βp		0.652	0.679	0.630	0.373	0.959	0.190	0.189	0.195
li		0.755	1.030	0.579	0.789	0.996	0.784	0.778	0.785
Fig. 4.1 ( )		(a)	(b)	(c)	(d)	(e)	(f)	(g)	(h)
Rp	Equilib.(m)	3.3682	3.3699	3.3688	3.3680	3.2680	3.1707	3.4051	2.8499
	TOLFEX(m)	3.3643	3.3701	3.3599	3.3636	3.1546	3.1546	3.4213	2.8932
	Error(mm)	-3.9	+0.2	-8.9	-4.5	-5.0	16.1	16.2	43.3
Zp	Equilib.(m)	0.2105	0.0980	0.2206	-.0688	0.1787	-.2156	0.3131	-.0056
	TOLFEX(m)	0.2113	0.0965	0.2151	-.0728	0.1752	-.1998	0.2660	-.0131
	Error(mm)	-9.2	-1.4	-5.5	15.7	-3.5	15.8	-47.1	-7.5
Λ	Equilib.(m)	1.030	1.194	0.9196	0.7493	1.4570	0.5824	0.5785	0.5885
	TOLFEX(m)	1.038	1.237	0.8839	0.7795	1.4030	0.4930	0.9042	1.2430
	Error(%)	+0.7	+3.6	-3.8	+4.0	-3.7	-15.3	-56.3	+111.2
Rx	Equilib.(m)	3.0792	3.0792	3.0792	3.0792				
	TOLFEX(m)	3.0700	3.0700	3.0800	3.0900				
Zx	Equilib.(m)	-1.449	-1.449	-1.522	-1.486				
	TOLFEX(m)	-1.422	-1.443	-1.445	-1.487				

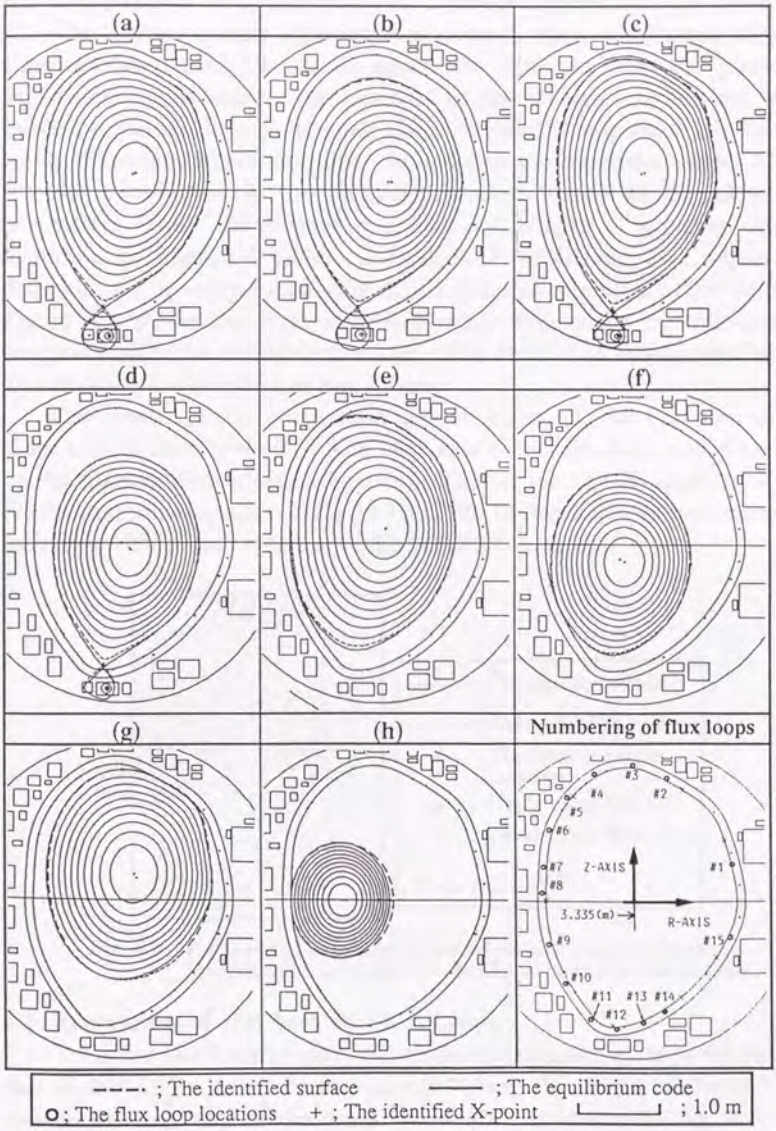

Fig. 4.1 Identified JT-60U Plasma Shapes by the TOLFEX Method Compared with the Output of the Equilibrium Code

4.2 Comparison with the Filament-Current Approximation Method

The filament-current approximation method, where six filament currents simulate the plasma current, is essentially different from the proposed TOLFEX method because the locations of the filament currents are fixed inside the plasma surface. In other words, the identifiable shape is restricted by the filament current locations. In contrast, the expansion center of the toroidal coordinates in the TOLFEX method is one of the identified parameters. Thus, the various positions and shapes of plasmas can be identified, as mentioned earlier. More than 15 calculations were required to determine the optimum locations of the six filament currents for identification. Figure 4.2 shows the final identified shape determined by this method compared with the equilibrium shape. (The same case determined by the TOLFEX method is shown in Fig. 4.1(a).)

The results of this comparison indicated that, (1) the precision of the shape reproduction by the TOLFEX method is almost the same as the best case by the filament-current approximation method in the JT-60U application and (2) the performance index J (Eq. (3.3)) of the filament-current approximation method is 20% greater than that of the TOLFEX method.

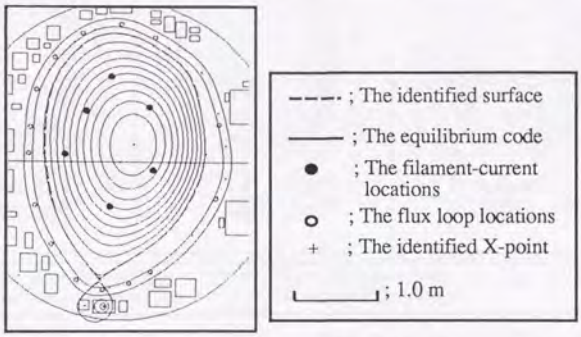

Fig. 4.2 The Identified Shape Determined by the Six-Filament-Current Approximation Compared with the Output of the Equilibrium Code

4.3 Evaluation of the Loss of Flux Loops

Though a flux loop is one of the simplest diagnostic devices, the case of loss of flux loops should be considered. Fifteen flux loops are located just outside the first wall of the vessel in JT-60U, as shown in Fig. 4.1. The necessary number of sensors is thirteen, one being a Rogowski coil. The unknown quantities are the coefficients of the seven eigenfunctions, the coefficients of the four PF-coil flux functions and the expansion center (R_0,

Z_0). Figure 4.3 shows the TOLFEX-identified shapes with the loss of one, two and three loops, respectively. Of significant importance, in the second case of Fig. 4.3 there is no loop on the third round (120°) of the wall on the poloidal cross-section. The resultant deviation, however, is not as great as might be expected. Table 4.2 shows the errors for several parameters. It follows that the TOLFEX method is robust against the loss of flux loops.

Table 4.2 Identification Errors Resulting from the Loss of Flux Loops

Shape parameters	Equilib. code output (m)	Number of the unused flux loops and difference from the equilibrium code (mm)			
		0	1	2	3
Rp	3.3682	-3.9	-17.7	-13.3	-12.4
Inner surface	2.3851	-9.9	+1.0	-1.1	+5.4
Outer surface	4.3513	+1.4	-36.4	-25.5	-30.2
Zp	0.2105	-9.2	-15.0	-14.9	-11.5
# of unused flux loops		none	#1	#1, 15	#1, 7, 13

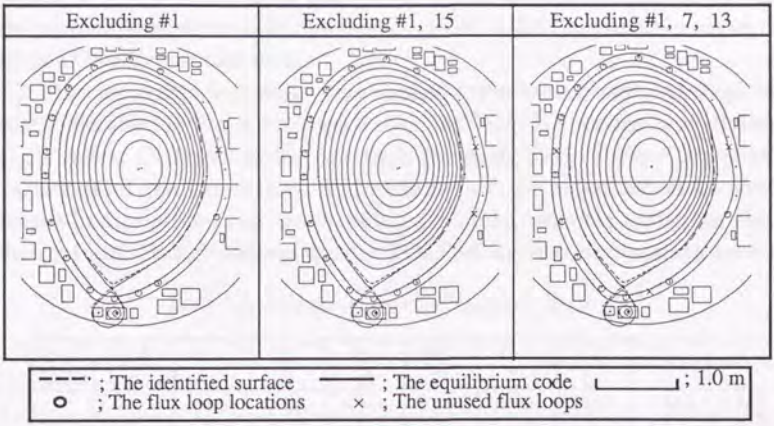

Fig. 4.3 The Identified JT-60U Plasma Shape by the TOLFEX Method for the Cases of the Loss of One, Two and Three Flux Loops

4.4 Evaluation of Noise Resistance

In the discussion above, the input data of the flux loops and the Rogowski coil to the TOLFEX method are identical to the output data from the equilibrium code. However, a condition where signal processing is ideally performed and no electromagnetic noise exists cannot be presumed. Thus, random noise should be included in the input data to the TOLFEX method for investigation of actual use. The applied noise is as follows:

(1) Rogowski coil

Assume 1% of the signal is random noise,

$$Ip^{noise} = Ip^{eq}\{1.0 + N(0.0, 0.01)\}, \qquad (4.1)$$

where Ip^{noise} is the input data to the TOLFEX method and Ip^{eq} is the output data from the equilibrium code. N(0.0, 0.01) expresses random noise having Gaussian distribution with m (mean value) = 0.0 and σ (standard deviation) = 0.01.

(2) Flux loop

A flux loop signal is produced by integrating the difference voltage of a flux loop from a fixed common reference flux loop. It is assumed that the largest signal to noise (S/N) ratio is 1000:1 for the pair of flux loops with the largest signal value. The S/N ratio of a flux loop with a smaller value becomes less than 1000:1, and thus the adopted supposition is rather severe. Now supposing the #8 loop is a common reference flux loop and the difference between the #8 and #M loops produces the largest signal, then

$$\phi^{noise}(i) = \phi^{eq}(i) + \{\phi^{eq}(M) - \phi^{eq}(8)\}\ N(0.0, 0.001), \qquad (4.2)$$

where $\phi^{noise}(i)$ is the input data to the TOLFEX method and $\phi^{eq}(i)$ is the output data from the equilibrium code. N(0.0, 0.001) expresses random noise having Gaussian distribution.

The input data with noise were applied to the same plasmas as those in the cases identified in Fig. 4.1. In each case, the TOLFEX method was performed eight times. Different noise was included each time. Table 4.3 shows the variations of the parameters. The variation of the major radius in case (h) (small limiter plasma) is ~5 cm, but in the other cases the variations are less than ± 1 cm. Thus, it follows that the TOLFEX method is robust against noise.

Table 4.3. Variation of the Parameters with Noise

Item \ Fig.4.1	(a)	(b)	(c)	(d)	(e)	(f)	(g)	(h)
Divert./Limit.	D	D	D	D	L	L	L	L
Ip	6 MA	6 MA	6 MA	2 MA	6 MA	4 MA	2 MA	1 MA
Rp variation	+5/-1	+2/0	+4/-2	+4/-1	+1/0	+3/-2	0/-2	+35/-70
Zp variation	+3/-10	+2/-3	+6/-5	+5/-1	+7/-3	+9/-3	+5/-2	+14/-5

variation (mm) ≡ {(data with noise) - (data without noise)}
(maximum variarion)/(minimum variation)

5. Discussion

Toroidal coordinates were first applied to an analytical solution of the G-S equation for the D-shape tokamak plasmas of the ISX-B device by Lee and Peng [5]. The identifiable shape in this solution may be extremely restricted because the point (R_0, Z_0) is fixed, as a result of the evaluation of the TOLFEX (toroidal-coordinates Legendre-Fourier expansion) method proposed in this chapter.

The method proposed by Lee and Peng [5] has the following differences from the TOLFEX method.

Dif. 1 Flux figures of the PF coils are not used.

Dif. 2 Plasma current is not taken into account.

Dif. 3 An artificial constraint on the coefficients of eigenfunctions is applied,

Dif. 4 A constant parameter must be identified.

Dif. 5 Only magnetic probe signals are used.

The peculiarity of the ISX-B device seems to make the need for PF coil flux figure unnecessary (Dif. 1). The coils for maintaining a D-shape plasma create a flux field similar to the eigenfunction Q·cos,m=3. Therefore, all of the flux fields produced by the PF coils can be expressed by eigenfunctions. That is probably why the flux figures of the PF coils are not necessary for the identification. Concerning Dif. 2, the precision of the TOLFEX method deteriorates in the JT-60U application without the use of a plasma current value. The coefficient of the eigenfunction P·cos,m=0 may include a large identification error if plasma current data are not utilized. This type of plasma flux figure uniformly increases or decreases the entire identified figure, see Fig. 2.1. The constant parameter, Dif. 4, can correct the identification error to some extent. Dif. 3 and Dif. 4 are never derived from the analytical solutions of PDEs, but they seem to adjust the flux figure. Dif. 5 corresponds to the solution with the Neumann boundary condition, where the solution exists uniquely. This is similar to that of the Dirichlet condition. In applications with magnetic probes, however, the average magnetic intensity along the axis is measured. This measurement includes the error due to probe direction.

Next, we estimate the required memory size and computation speed for the execution of the TOLFEX method by a computer in real time. "Table-look-up procedures" should be employed for the real-time calculation of the Legendre function. The results of calculations performed without the observed plasma current and flux data should be executed before the discharge and should be stored in the computer memory in tabular form.

The search for (R_0,Z_0) requires the calculation of $J(r,z)$ and $\partial J(r,z)/\partial z$. The parameters **U**, **V**, W in Eq. (3.8) and their derivatives should be stored in tabular form. The flux calculations on the fixed limiter, the X-point search and the major radius calculation require the parameters **a** and b in Eq. (3.10), which should also be stored in tabular form. To estimate the requirements for a computer capable of performing these tasks, assume the range of (R_0,Z_0) is restricted to remain inside the 0.5m-radius circle whose center is that of the vacuum vessel and that the number of flux loops is 15. The memory size

required is estimated to be about 15 Mbytes. The longest calculation time needed will be to calculate J(r,z) and $\partial J(r,z)/\partial z$; roughly 400 instructions are required. If the calculation cycle time of the processor is 0.1 μsec, 40 μsec will be needed for one J(r,z) or $\partial J(r,z)/\partial z$ calculation. Fifty iterations are assumed to be required for the determination of (R_0,Z_0). Thus, it takes 2.0 msec to perform the calculation. The number of processors should be determined according to the required cycle time of control.

6. Concluding Remarks

The proposed method in this chapter —TOLFEX method — is summarized as follows:

(1) The method can identify the shape of an asymmetric divertor plasma without information on the expansion center (R_0, Z_0) because the point (R_0, Z_0) can be determined through "the two-step least squares method." It can also identify the shape of a small circular plasma .

(2) The method does not need magnetic probes. By employing a discrete-point boundary condition and a finite series of flux eigenfunctions, the plasma shape can be accurately reproduced.

(3) The method can take eddy currents into consideration. Information of uniform field produced by the eddy currents is contained in the eigenfunctions having Legendre functions of the second kind. The flux produced by axisymmetric eddy currents can be added to the members of the eigenfunctions.

(4) The method can be executed in real time where a table-look-up procedure is applied for calculation. It is possible to apply this method to feedback control and real-time visualization.

(5) Since (R_0,Z_0) is identified close to the magnetic axis, Z_0 can be used as the vertical position. Feedback control for the vertical position can be started at the calculation step that determines (R_0,Z_0). Thus, a short control cycle can be utilized to suppress vertical instability.

(6) The method is robust against the loss of flux loops and the existence of signal noise.

References in Chapter II.1

[1] Aikawa,H. et al., "Derivation of plasma displacement in a tokamak from magnetic probe signals," Japanese Journal Applied Physics vol.15 (1976)

p.2031 & p.2479.
[2] Blum,J., "Numerical simulation and optimal control in plasma physics with application to tokamaks," John Wiley and Sons (1988).
[3] Hosogane,N. et al., "Method for measuring divertor configuration parameters for feedback control in JT-60," Nuclear Fusion vol.26 (1986) p.657.
[4] Lao,L.L. et al., "Separation of βp and li in tokamaks of non-circular cross-section," Nuclear Fusion vol.25 (1985) p.1421.
[5] Lee,D.K. & Peng,Y.-K.M., "An approach to rapid plasma shape diagnostics in tokamaks," Journal of Plasma Physics vol.25 (1981) p.161.
[6] Alladio,F. & Crisanti,F., "Analysis of MHD equilibria by toroidal multipolar expansions," Nuclear Fusion vol.26 (1986) p.1143
[7] Luxon,J.L. & Brown,B.B., "Magnetic analysis of non-circular cross-section tokamaks," Nuclear Fusion vol.22 (1982), p.813.
[8] Mukhovatov,V.S. and Shafranov,V.D., "Plasma equilibrium in a tokamak," Nuclear Fusion vol.11 (1971) p.605.
[9] Voss,D.E. et al., "Application of numerical equilibrium calculations to positioning of the Princeton Large Torus plasma," Princeton Plasma Physics Laboratory Report PPPL-1483 (1978).
[10] Reusch,M.F. & Neilson,G.H., "Finite order polynomial moment solutions of the homogeneous Grad-Shafranov equation," ibid. PPPL-2072 (1984).
[11] Schneider,F., "Novel method of determining the plasma position and its application to the ASDEX feedback system," Proceedings of 10th Symposium on Fusion Technology, Padova (1978), p.1013.
[12] Swain,D.W. & Neilson,G.H., "An efficient technique for magnetic analysis of non-circular, high-beta tokamak equilibria," Nuclear Fusion vol.22 (1982), p.1015.
[13] Horiike,H. et al., "Present status of JT-60 Upgrade," Proceedings of 13th Symposium on Fusion Engineering, Knoxville (1989) p.1049.
[14] Morse,P.M. & Feshbach,H., "Methods of theoretical physics: Part I&II," McGrow-Hill Book Company Inc.(1953).
[15] Deshko,G.N., et al., "Determination of the plasma column shape in a tokamak from magnetic measurements," Nuclear Fusion vol.23 (1983) p.1309.
[16] Shafranov,V.D., "Determination of the parameters βı and li in a tokamak for arbitrary shape of plasma pinch cross-section," Plasma Physics vol.13 (1971) pp.757-762.

II.2 Tokamak Plasma Shape Identification Based on Boundary Integral Equations

1. Introduction

To conduct experiments and data evaluation properly in tokamak devices, plasma shape identification is needed for plasma equilibrium control and analysis. Various methods to identify these shapes have been proposed[1]. However, a method called "filament-current-approximation (FCA)[2]" seems to be most frequently applied to tokamaks. This method uses several filament-current-coils to express the vacuum magnetic field produced by the plasma current. For such a simple approximation, this method reproduces the shape comparatively well using only magnetic measurements. In contrast, methods based on the analytical solution of partial differential equations (PDEs) such as the "Legendre-Fourier expansion (LFE)[3]", the "multipole expansion[4]", etc., give poor identifications for plasmas with certain shapes or current profiles[3]. This results from the small number of sensors employed and also because numerical limitations allow only calculation of the first few series in solution formulas that are composed of an infinite series of eigenfunctions. Full equilibrium analysis[5] with the plasma current/pressure profile formulas requires knowledge of the shape. The premise that the predetermined formulas for this analysis can match the various states of plasmas is still questionable. Furthermore, the existing methods, FCA and LFE, cannot accurately identify the shape of a highly-elongated ($\kappa \approx 2.2$) ITER (International Thermonuclear Experimental Reactor[6]) plasma. The reason for this is not clear; it seems the identification of the plasma shape is not fully understood. In this chapter, a necessary condition for plasma shape identification is discussed from the view points of conceptual mathematics and numerical computation. It is then confirmed that the method utilized for derivation of the condition gives shape reproduction with only the necessary condition in application to the JT-60 Upgrade (JT-60U) and ITER.

First, conceptual and theoretical considerations of shape identification are discussed in Section 2. Some techniques of the numerical computation used in the method are described in Section 3. Application to tokamak plasmas in JT-60U and ITER along with several discussions are presented in Section 4.

2. Tokamak Plasma Shape Identification Concept

It is well known that a tokamak plasma is so light that it is considered to preserve its equilibrium state. The problem of concern is, therefore, to identify the static magnetic field that results from currents flowing in both the plasma and poloidal field (PF) coils. Magnetic measurement data are presumed for this identification because magnetic sensors are at present passably reliable in a tokamak and should also be in the future. These sensors measure the magnetic or flux fields in the vacuum around a plasma. Since the plasma surface is a border surface of the vacuum region, complete identification of the magnetic fields in this vacuum region would then give the identification of the plasma shape. Is this possible in an actual system? What kinds of magnetic sensors are necessary? The answer to these questions are discussed in this section.

2.1 Topological Concept of the Problem and Formulation of the Equations

The quantities of current density ($\mathbf{j}$) and magnetic flux intensity ($\mathbf{B}$) are connected by the following static Maxwell's equations:

$$\text{rot } \mathbf{B} = \mu_0 \mathbf{j}, \tag{2.1}$$

$$\text{div } \mathbf{B} = 0. \tag{2.2}$$

By introducing the vector potential $\mathbf{A}$ ($\mathbf{B}=\text{rot}\mathbf{A}$) from Eq. (2.2), Eq. (2.1) becomes:

$$\text{rot rot } \mathbf{A} = \mu_0 \mathbf{j}. \tag{2.3}$$

It is assumed that all the quantities are axisymmetric. Now the flux function ϕ is defined as $\phi \equiv r \cdot A_\omega$, where A_ω is a toroidal component of the vector $\mathbf{A}$, and r is the distance from the axis in cylindrical coordinates. Then Eq. (2.3) can be converted to the following scalar equation:

$$\text{div } [(\text{grad } \phi)/r^2] = -\mu_0 j_\omega / r, \tag{2.4}$$

where j_ω is a toroidal component of the vector $\mathbf{j}$. The variable j_ω can be expressed by using the pressure and current profile functions, $p(\phi)$ and $I(\phi)$, in terms of the flux function ϕ:

$$j_\omega = (\mu_0/r)/2 \cdot dI^2/d\phi + r \cdot dp/d\phi. \tag{2.5}$$

The substitution of Eq. (2.5) for the right hand side of Eq. (2.4) yields the Grad-Shafranov equation. For a vacuum region, j_ω is set to zero in Eq. (2.4), and the following equation is then obtained[7]:

$$\text{div}\,[(\text{grad}\,\phi)/r^2] = 0. \qquad (2.6)$$

This equation is classified as an elliptic nonlinear homogeneous second-order PDE. In general, a boundary value problem for an elliptic second-order PDE is known to give a unique solution with a Dirichlet or a Neumann condition on a closed boundary[8]. However, as the plasma current profile is unknown, the concerned analytical region is a doughnut-shaped area surrounding the plasma. This topological concept is shown in Fig. 2.1. It seems to be unclear whether a uniqueness of solution for a general elliptic second-order PDE still holds in such a region that is not simply connected. However, the analytical solution of Eq. (2.6), based on the method of separation of variables, gives two kinds of eigenfunctions, one of which has a singular point[3]. This suggests the existence of a unique solution for Eq. (2.6) in such a region that is not simply connected, with a Dirichlet or a Neumann condition on a closed boundary. In fact, the shape identification method using those eigenfunctions gives a good result for low-κ plasmas[3].

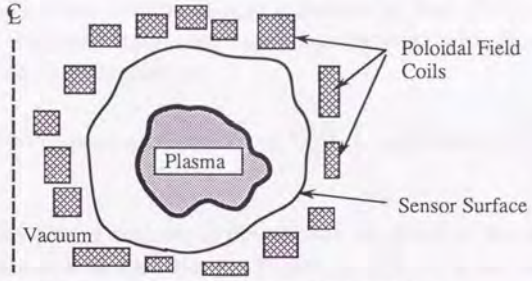

Fig. 2.1 Topological Concept of the Analytical Region

Now Eq. (2.4) is solved by converting Eq. (2.4) to the form of an integral equation using a Green function because this approach is most advantageous for a numerical solution of the concerned PDE. (The reason for this selection is explained in Appendix 1.) In the identity of the scalar functions, f and g:

$$\text{div}[f\cdot(\text{grad}\,g)/r^2] - \text{div}[g\cdot(\text{grad}\,f)/r^2] = f\cdot\text{div}[(\text{grad}\,g)/r^2] - g\cdot\text{div}[(\text{grad}\,f)/r^2], \qquad (2.7)$$

$\phi(\mathbf{y})$ and $G(\mathbf{x}, \mathbf{y})$ are substituted for f and g, respectively. The function G is the Green function between two points, $\mathbf{x}$ and $\mathbf{y}$, in an axisymmetric geometry. The points $\mathbf{x}$ and $\mathbf{y}$ are defined as (r_x, z_x) and (r_y, z_y), respectively in cylindrical coordinates. The function G is then expressed as:

$$G(\mathbf{x}, \mathbf{y}) = G(r_x, z_x, r_y, z_y) = \frac{4}{k}\sqrt{r_x \cdot r_y}\left\{\left(1 - \frac{k^2}{2}\right) K(k) - E(k)\right\}, \tag{2.8}$$

where K and E are the complete elliptic integrals of the first and second kinds, and $k^2 \equiv 4 \cdot r_x \cdot r_y / \{(r_x + r_y)^2 + (z_x - z_y)^2\}$. Furthermore, as this Green function is identical with the 0-th order eigenfunction of Eq. (2.6), the following equation holds:

$$\mathrm{div}\,[(\mathrm{grad}\, G(\mathbf{x}, \mathbf{y}))/r_y^2] = \gamma \cdot \delta(\mathbf{x}, \mathbf{y}), \tag{2.9}$$

$$\gamma \equiv \lim_{\substack{\text{volume } \Omega \to 0 \\ \mathbf{x} \subset \Omega}} \int_\Omega \mathrm{div}\left[\frac{\mathrm{grad} G(\mathbf{x}, \mathbf{y})}{r_y^2}\right] \cdot dV(\mathbf{y}) = -8\pi^2 \quad , \tag{2.10}$$

where $\delta(\mathbf{x}, \mathbf{y})$ is the delta function, $\delta(\mathbf{x}, \mathbf{y}) \equiv [0\ (\mathbf{x} \neq \mathbf{y}),\ \infty\ (\mathbf{x} = \mathbf{y})]$,

$$\int_\Omega \phi(\mathbf{y}) \cdot \delta(\mathbf{x}, \mathbf{y})\, d\mathbf{y} = \phi(\mathbf{x}), \quad \mathbf{x} \subset \Omega \quad , \tag{2.11}$$

and $dV(\mathbf{y})$ is the infinitesimal volume element at point $\mathbf{y}$. After integrating the identity Eq. (2.7) in the volume Ω with respect to $\mathbf{y}$, Eqs. (2.4), (2.9), (2.11) and the Gauss integral formula are taken into account with $\Omega \supset \mathbf{x}$. Then the solution of Eq. (2.4) is obtained as:

$$\sigma \cdot \phi(\mathbf{x}) = \int_{\partial\Omega} [G(\mathbf{x}, \mathbf{y}) \cdot \mathrm{grad}\phi(\mathbf{y}) - \phi(\mathbf{y}) \cdot \mathrm{grad} G(\mathbf{x}, \mathbf{y})] \cdot \frac{dS(\mathbf{y})}{r_y^2} + \int_\Omega \mu_0 j(\mathbf{y}) \cdot G(\mathbf{x}, \mathbf{y}) \cdot \frac{dV(\mathbf{y})}{r_y} \quad , \tag{2.12}$$

where $\partial\Omega$ is the closed surface of the volume Ω, $dS(\mathbf{y})$ is the infinitesimal surface element vector at the point $\mathbf{y}$, $dS(\mathbf{y}) \equiv \mathbf{n}(\mathbf{y}) \cdot dS(\mathbf{y})$, $\mathbf{n}$ is the vector normal to the surface $\partial\Omega$ in the direction away from Ω, $j(\mathbf{y})$ is the current density distribution involved in the region Ω, and σ is a constant defined by:

$$\sigma = -\gamma \cdot \theta,\ \theta = \{1\ (\Omega \supset \mathbf{x}),\ 1/2\ (\partial\Omega \supset \mathbf{x})^{[9]},\ 0\ (\text{the area excluding } (\Omega + \partial\Omega) \supset \mathbf{x})\}.$$

Equation (2.12) signifies that if the current distribution in region Ω is known, the solution can be exactly expressed with the Dirichlet ($\phi(\mathbf{y})$) and Neumann (grad $\phi(\mathbf{y})$) boundary conditions on the surface $\partial\Omega$. The identifiability condition for tokamak plasma shape using this solution is discussed in the following subsection.

2.2 A Necessary Condition for Plasma Shape Identification

Equation (2.12) requires knowledge of j(y) in the region Ω. As the plasma current distribution was not known at the time of shape identification, the plasma current cannot be taken as j(y) for Eq. (2.12). It is assumed that PF coils and other current distributions, except plasma current, are known. This does not degrade the conceptual discussion of shape identification. This is because the field produced by unobservable currents such as eddy currents is negligibly small when compared with the field produced by the plasma current. The exception is for the case of short periods of current build-up and disruption[10].

Three closed curved surfaces nested one within another are now defined in the axisymmetric analytical region. On the poloidal cross section, these surfaces show the nested closed curved surfaces illustrated in Fig. 2.2.

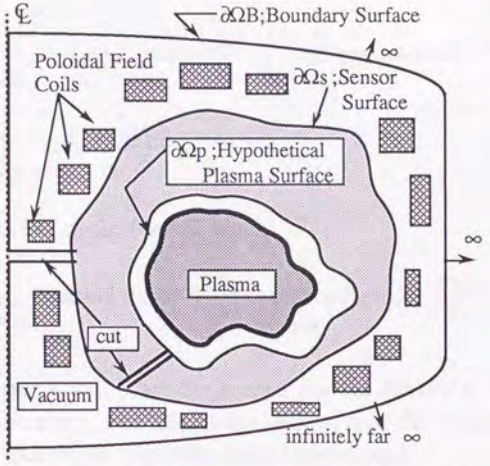

Fig. 2.2 Topological Concept of the Closed Surfaces and Integral Routes

The first surface is the boundary surface, $\partial\Omega_B$, which contains the whole region of concern. The second surface is the sensor surface, $\partial\Omega_S$, along which the sensors are located and which is contained by $\partial\Omega_B$. The third surface is the hypothetical plasma surface, $\partial\Omega_P$, that contains the plasma column and is contained by $\partial\Omega_S$. The area bounded by the surface $\partial\Omega_1$ and $\partial\Omega_2$ is denoted by $\Omega_{1\text{-}2}$. Equation (2.12) is applied to two regions, $\Omega_{B\text{-}S}$ and $\Omega_{S\text{-}P}$, which do not involve the plasma. Then $\partial\Omega_B$ is subsequently moved infinitely far from the

concerned area. With respect to $\mathbf{y}$ on the central axis, $G(\mathbf{x}, \mathbf{y})=0$ and $\mathrm{grad}G(\mathbf{x},\mathbf{y})=\mathbf{0}$. By taking into account the following limitation:

$$\lim_{\partial\Omega_B\to\infty}\int_{\partial\Omega_B}[G\cdot\mathrm{grad}\phi-\phi\cdot\mathrm{grad}G]\cdot\frac{dS(y)}{r_y^2}=0 \quad , \tag{2.13}$$

the surface integral on $\partial\Omega_B$ in Eq. (2.12) vanishes. Consequently, the solutions for Eq. (2.4) in the regions, $\Omega_{B\text{-}S}$ and $\Omega_{S\text{-}P}$, are as follows:
For $\mathbf{x}\subseteq\Omega_{B\text{-}S}$,

$$\sigma\cdot\phi(\mathbf{x})=\int_{\partial\Omega_S}[G\cdot\mathrm{grad}\phi-\phi\cdot\mathrm{grad}G]\cdot\frac{dS(y)}{r_y^2}+\int_{\Omega_{B\text{-}S}}\mu_0 j_c\cdot G\cdot\frac{dV(y)}{r_y} \quad . \tag{2.14}$$

For $\mathbf{x}\subseteq\Omega_{S\text{-}P}$,

$$\sigma\cdot\phi(\mathbf{x})=\int_{\partial\Omega_P}[G\cdot\mathrm{grad}\phi-\phi\cdot\mathrm{grad}G]\cdot\frac{dS(y)}{r_y^2}-\int_{\partial\Omega_S}[G\cdot\mathrm{grad}\phi-\phi\cdot\mathrm{grad}G]\cdot\frac{dS(y)}{r_y^2}$$
$$+\int_{\Omega_{P\text{-}S}}\mu_0 j_v\cdot G\cdot\frac{dV(y)}{r_y} \quad . \tag{2.15}$$

By using Eq. (2.14), again for $\mathbf{x}\subseteq\Omega_{B\text{-}P}$,

$$\sigma\cdot\phi(\mathbf{x})=\int_{\partial\Omega_P}[G\cdot\mathrm{grad}\phi-\phi\cdot\mathrm{grad}G]\cdot\frac{dS(y)}{r_y^2}+\int_{\Omega_{P\text{-}B}}\mu_0(j_c+j_v)\cdot G\cdot\frac{dV(y)}{r_y} \quad . \tag{2.16}$$

In these equations j_c and j_v are the known current density in the regions $\Omega_{B\text{-}S}$ and $\Omega_{S\text{-}P}$, respectively. For $dS(y)\equiv\mathbf{n}(y)\cdot dS(y)$, $\mathbf{n}$ is the vector normal to the surface $\partial\Omega_S$ or $\partial\Omega_P$ in the direction toward the plasma.

The integral along the curved surface $\partial\Omega_S$ in Eq. (2.14) requires that the values of $\phi(y)$ and $\mathrm{grad}\phi(y)$ be measured. The quantity $\phi(y)$ is directly measured by the time-integral of the voltage signal from a one-turn flux loop. The quantity B_t denotes a tangential component of a flux intensity vector to the curved surface $\partial\Omega_S$, and B_t can be expressed in terms of ϕ as $B_t=\mathrm{grad}\phi\cdot\mathbf{n}/r_y$. The signal from a magnetic probe located along $\partial\Omega_S$ gives $\mathrm{grad}\phi\cdot\mathbf{n}/r_y$. Therefore, ϕ and B_t can be measured by magnetic sensors.

An infinite series formula is introduced for further discussion. $K(\alpha,\beta)$ is a bounded and smooth function, except in the case where $\alpha=\beta$ and $q(\beta)$ is a

smooth function in the integral domain Ω. If α and β are involved in Ω, and if the integral of $K_{(\alpha,\beta)}$ with respect to β is bounded, i.e. $\int K_{(\alpha,\beta)}d\beta < \infty$, then:

$$\int_a^b K(\alpha, \beta)\cdot q(\beta)\, d\beta = \sum_{i=1}^{\infty} w(h_i, \alpha, \beta_i)\cdot q(\beta_i) \quad , \tag{2.17}$$

(see Appendix 2) where h_i is the i-th infinitesimal length for the definite integral in the interval [a,b]. By using a sufficiently large number N for division of the integral interval, Eq. (2.17) can be converted to:

$$\int_a^b K(\alpha, \beta)\cdot q(\beta)\, d\beta = \sum_{i=1}^{N} w(h_i, \alpha, \beta_i)\cdot q(\beta_i) + \delta(\alpha, N) \quad , \tag{2.18}$$

where $\delta(\alpha, N)$ is a sufficiently small function compared with the first term of the right hand side of Eq. (2.18). This function is presumed to decrease monotonously as N increases, i.e. $\delta(\alpha, N\to\infty) \to 0$.

Now, let the numbers for division of the curved surfaces $\partial\Omega_S$ and $\partial\Omega_P$ be N and M, respectively, and $N \geq M$. Equations (2.14) and (2.16) are then expressed as infinite series formulas by utilizing Eq. (2.18), where the residual function δ denotes the total amount of residues produced by all integrals in Eq. (2.14), (2.15) or (2.16). In Eq. (2.14), by bringing **x** infinitely close to the boundary $\partial\Omega_S$ from the inside, we obtain:

$$\phi(\mathbf{x}) = \sum_{i=1}^{N} W_1^1(\mathbf{x}, y_i)\cdot\phi(y_i) + \sum_{i=1}^{N} W_2^1(\mathbf{x}, y_i)\cdot Bt(y_i) + W_3^1(\mathbf{x}) + \delta^1(\mathbf{x}, N), \quad \mathbf{x}\subseteq\partial\Omega_S,\ y_i\subseteq\partial\Omega_S \quad . \tag{2.19}$$

Similarly, in Eq. (2.16) **x** is brought infinitely close to $\partial\Omega_S$ and $\partial\Omega_P$ from the inside, and then:

$$\phi(\mathbf{x}) = \sum_{i=1}^{M} W_1^2(\mathbf{x}, z_i)\cdot\phi(z_i) + \sum_{i=1}^{M} W_2^2(\mathbf{x}, z_i)\cdot Bt(z_i) + W_3^2(\mathbf{x}) + \delta^2(\mathbf{x}, M), \quad \mathbf{x}\subseteq\partial\Omega_S,\ z_i\subseteq\partial\Omega_P \quad , \tag{2.20}$$

$$\phi(\mathbf{x}) = \sum_{i=1}^{M} W_1^3(\mathbf{x}, z_i)\cdot\phi(z_i) + \sum_{i=1}^{M} W_2^3(\mathbf{x}, z_i)\cdot Bt(z_i) + W_3^3(\mathbf{x}) + \delta^3(\mathbf{x}, M), \quad \mathbf{x}\subseteq\partial\Omega_P,\ z_i\subseteq\partial\Omega_P \quad . \tag{2.21}$$

Equation (2.19) (or Eq. (2.14)) expresses the relation between ϕ on $\partial\Omega_S$ and Bt on $\partial\Omega_S$. Equation (2.20) expresses the relation between ϕ on $\partial\Omega_S$, and ϕ and Bt on $\partial\Omega_P$. Equation (2.21) expresses the relation between ϕ on $\partial\Omega_P$ and Bt on $\partial\Omega_P$. As Eqs. (2.19)~(2.21) are linear, they can be composed as vector equations with matrix coefficients. According to the existence theorems for the solution of the Fredholm integral equation of the first kind, no solution exists

except for the special case within analytical discussions[*]. However, no difficulty is encountered in the discretized Fredholm equation.

By $\mathbf{x}=\mathbf{y}_i$ (i=1,2,..,N) in Eqs. (2.19) and (2.20), two sets of simultaneous N equations are obtained. Similarly, by $\mathbf{x}=\mathbf{z}_i$ (i=1,2,..,M) in Eq. (2.21), a set of simultaneous M equations is obtained. The three sets of the vector equations are then expressed as:

$$\phi^S = \mathbf{A}_1\cdot\phi^S + \mathbf{B}_1\cdot\mathbf{Bt}^S + \mathbf{c}_1 + \mathbf{d}_1, \tag{2.22}$$
$$\phi^S = \mathbf{A}_2\cdot\phi^P + \mathbf{B}_2\cdot\mathbf{Bt}^P + \mathbf{c}_2 + \mathbf{d}_2, \tag{2.23}$$
$$\phi^P = \mathbf{A}_3\cdot\phi^P + \mathbf{B}_3\cdot\mathbf{Bt}^P + \mathbf{c}_3 + \mathbf{d}_3, \tag{2.24}$$

where the vectors and matrix coefficients are defined as follows:

$$\phi^S \equiv {}^t[\,\phi(\mathbf{y}_1),\ \phi(\mathbf{y}_2),\ \phi(\mathbf{y}_3),\ldots,\ \phi(\mathbf{y}_N)] \in \mathbf{R}^{N\times 1},$$
$$\phi^P \equiv {}^t[\,\phi(\mathbf{z}_1),\ \phi(\mathbf{z}_2),\ \phi(\mathbf{z}_3),\ldots,\ \phi(\mathbf{z}_M)] \in \mathbf{R}^{M\times 1},$$
$$\mathbf{Bt}^S \equiv {}^t[\,\mathrm{Bt}(\mathbf{y}_1),\ \mathrm{Bt}(\mathbf{y}_2),\ \mathrm{Bt}(\mathbf{y}_3),\ldots,\ \mathrm{Bt}(\mathbf{y}_N)] \in \mathbf{R}^{N\times 1},$$
$$\mathbf{Bt}^P \equiv {}^t[\,\mathrm{Bt}(\mathbf{z}_1),\ \mathrm{Bt}(\mathbf{z}_2),\ \mathrm{Bt}(\mathbf{z}_3),\ldots,\ \mathrm{Bt}(\mathbf{z}_M)] \in \mathbf{R}^{M\times 1},$$

$$\mathbf{A}1(i,j) \equiv \left[W_1^1(\mathbf{y}_i,\ \mathbf{y}_j)\right] \in \mathbf{R}^{N\times N},\quad \mathbf{B}1(i,j) \equiv \left[W_2^1(\mathbf{y}_i,\ \mathbf{y}_j)\right] \in \mathbf{R}^{N\times N},\quad \mathbf{c}1 \equiv {}^t\left[W_3^1(\mathbf{y}_1),\ W_3^1(\mathbf{y}_2),\ldots,W_3^1(\mathbf{y}_N)\right] \in \mathbf{R}^{N\times 1},$$
$$\mathbf{A}2(i,j) \equiv \left[W_1^2(\mathbf{y}_i,\ \mathbf{z}_j)\right] \in \mathbf{R}^{N\times M},\quad \mathbf{B}2(i,j) \equiv \left[W_2^2(\mathbf{y}_i,\ \mathbf{z}_j)\right] \in \mathbf{R}^{N\times M},\quad \mathbf{c}2 \equiv {}^t\left[W_3^2(\mathbf{y}_1),\ W_3^2(\mathbf{y}_2),\ldots,W_3^2(\mathbf{y}_N)\right] \in \mathbf{R}^{N\times 1},$$
$$\mathbf{A}3(i,j) \equiv \left[W_1^3(\mathbf{z}_i,\ \mathbf{z}_j)\right] \in \mathbf{R}^{M\times M},\quad \mathbf{B}3(i,j) \equiv \left[W_2^3(\mathbf{z}_i,\ \mathbf{z}_j)\right] \in \mathbf{R}^{M\times M},\quad \mathbf{c}3 \equiv {}^t\left[W_3^3(\mathbf{z}_1),\ W_3^3(\mathbf{z}_2),\ldots,W_3^3(\mathbf{z}_M)\right] \in \mathbf{R}^{M\times 1},$$

$$\mathbf{d}1 \equiv {}^t\left[\delta^1(\mathbf{y}_1,N),\ \delta^1(\mathbf{y}_2,N),\ldots,\delta^1(\mathbf{y}_N,N)\right] \in \mathbf{R}^{N\times 1},\quad \mathbf{d}2 \equiv {}^t\left[\delta^2(\mathbf{y}_1,M),\ \delta^2(\mathbf{y}_2,M),\ldots,\delta^2(\mathbf{y}_N,M)\right] \in \mathbf{R}^{N\times 1},$$
$$\mathbf{d}3 \equiv {}^t\left[\delta^3(\mathbf{z}_1,M),\ \delta^3(\mathbf{z}_2,M),\ldots,\delta^3(\mathbf{z}_M,M)\right] \in \mathbf{R}^{M\times 1}.$$

By elimination of $\mathbf{Bt}^P$ from Eqs. (2.23) and (2.24) using the method of least-squares, the following relations are obtained:

$$\phi^P = ({}^t\mathbf{F}\cdot\mathbf{F})^{-1}\cdot{}^t\mathbf{F}\cdot\{\phi^S + (\mathbf{B}_2\cdot\mathbf{B}_3^{-1}\mathbf{c}_3 - \mathbf{c}_2) + (\mathbf{B}_2\cdot\mathbf{B}_3^{-1}\mathbf{d}_3 - \mathbf{d}_2)\}, \tag{2.25}$$
$$\mathbf{F} \equiv \mathbf{A}_2 + \mathbf{B}_2\cdot\mathbf{B}_3^{-1}(\mathbf{I}_M - \mathbf{A}_3),\quad \mathbf{I}_M;\ \text{a unit matrix} \in \mathbf{R}^{M\times M},$$
$$\mathbf{Bt}^P = \mathbf{B}_3^{-1}(\mathbf{I}_M - \mathbf{A}_3)\cdot\phi^P - \mathbf{B}_3^{-1}\mathbf{c}_3 - \mathbf{B}_3^{-1}\mathbf{d}_3. \tag{2.26}$$

Eq. (2.22) can be rearranged as:

$$\phi^S = (\mathbf{I}_N - \mathbf{A}_1)^{-1}\cdot(\mathbf{B}_1\cdot\mathbf{Bt}^S + \mathbf{c}_1 + \mathbf{d}_1), \tag{2.27}$$
$$\mathbf{I}_N;\ \text{a unit matrix} \in \mathbf{R}^{N\times N}.$$

Matrix inversions in Eqs. (2.25), (2.26), and (2.27) can be calculated because the independence of the rows are preserved even for N and M$\to\infty$ (preserving

[*]; Classification of the integral equation types: $\mathbf{x}\to\partial\Omega$S in Eq. (2.14) and $\mathbf{x}\to\partial\Omega$P in Eq. (2.16) yield the boundary integral equations. These belong to the Fredholm integral equation of the second kind for the flux function ϕ and that of the first kind for the flux intensity Bt. The relation $\mathbf{x}\to\partial\Omega$s in Eq. (2.16) is the Fredholm integral equation of the first kind for both ϕ and Bt on $\partial\Omega$P. The Fredholm equation of the second kind has a unique solution, while that of the first kind does not have a solution except in a special case[11].

$N \geq M$). As the vectors of residuals $\mathbf{d}_1$, $\mathbf{d}_2$ and $\mathbf{d}_3$ monotonously converge to 0, ϕ^P and $\mathbf{Bt}^P$ converge to the real values. By substitution of ϕ^P and $\mathbf{Bt}^P$ into Eq. (2.16), a flux function value can be calculated at any point $\mathbf{x}$ outside $\partial\Omega_P$. Equation (2.27) implies that $\mathbf{Bt}^S$ on $\partial\Omega_S$ gives ϕ^S on $\partial\Omega_S$. Equations (2.25) and (2.26) imply that ϕ^S on $\partial\Omega_S$ gives $\mathbf{Bt}^P$ and ϕ^P on $\partial\Omega_P$. Therefore, intermediate Conclusion I results, which specifies that a necessary condition to identify the flux function in a vacuum region outside a plasma (see Fig. 2.2) is that either flux intensities tangential to the curved surface $\partial\Omega_S$ ($\mathbf{Bt}^S$) or flux function values at points on $\partial\Omega_S$ (ϕ^S) must be continuously given.

Conclusion I does not directly specify a condition to identify plasma shapes. However, it implies that the flux function values at all points in the vacuum region facing the plasma can be identified by magnetic measurements in a vacuum around the plasma. To advance the discussion, properties of the plasma outermost surface shall be confirmed. It is well known that either a limiter on the first wall of the vacuum vessel or an X-point, which is usually produced by the divertor coil, determines the outermost flux surface having a certain value of the flux function. If the flux function distribution in the poloidal cross section is compared to the "geographical altitude of a mountain," then the contour having the highest (or lowest) altitude in a vacuum around a plasma identifies the outermost flux surface.

The hypothetical plasma surface $\partial\Omega_P$ has been located to enclose the plasma. Now the solution of the integral equations by locating $\partial\Omega_P$ inside the plasma is considered. This corresponds to the identification of a different plasma that produces the same flux field outside a real plasma. Therefore, the identified flux field in the area between $\partial\Omega_P$ and a real plasma surface is no longer a reality. However, it can be proved that the identified flux field agrees with a real field outside a real plasma surface (see Appendix 3). As a result, a contour having the properties of the plasma surface in the region outside $\partial\Omega_P$ uniquely exists[#] and this contour is denoted by $\partial\Omega_{P^*}$. The quantities ϕ^{P^*} and $\mathbf{Bt}^{P^*}$ denote the flux function on $\partial\Omega_{P^*}$ and flux intensity tangential to the curved surface $\partial\Omega_{P^*}$, respectively. It is clear that $\mathbf{Bt}^{P^*}$ and ϕ^{P^*} are the result of the boundary integral equations where $\partial\Omega_{P^*}$ is an inner boundary surface—the hypothetical plasma surface. Thus, we obtain intermediate Conclusion II, which specifies that a closed surface having the properties of the plasma surface uniquely exists in the region outside the hypothetical plasma surface

[#]; If more than one contours exist having plasma surface properties, one of them must be a real plasma surface. The remaining contours must be inside a real plasma, because the exact flux field outside a real plasma has been solved. However, these remaining contours contradict the properties of the outermost plasma surface.

($\partial\Omega_{P^*}$) and that it can be determined by solving the boundary integral equations by letting $\partial\Omega_P$ be located within a plasma.

Considering intermediate Conclusions I and II, the following conclusion is finally reached: a necessary condition to identify the shape of the plasma surface is that either flux intensities tangential to the curved surface $\partial\Omega s$ ($\mathbf{Bt}^S$) or flux function values at points on $\partial\Omega s$ (ϕ^S) must be continuously given.

3. Calculation Algorithm and Techniques

In the previous section the identifiability condition is derived with the assumption of ideal measurement. In reality, however, magnetic sensors are located at irregular intervals on the wall of a vertically asymmetrical vacuum vessel. In this section, a more realistic algorithm is presented to calculate the flux function distribution in a vacuum around a plasma using a finite number of sensors. The calculation flow is first discussed, followed by several calculation techniques peculiar to this algorithm.

(1) Calculation flow

If the flux intensities tangential to the curved surface $\partial\Omega s$ on the poloidal cross section, $\mathbf{Bt}^S$, are given, the following three calculations are required. If the flux function values at points on $\partial\Omega s$, ϕ^S, are given, the first calculation is not performed.

Calculation 1: Input [$\mathbf{Bt}^S$ on $\partial\Omega s$] $\rightarrow$ Output [ϕ^S on $\partial\Omega s$].

Equation (2.27), the discretized equation of the boundary integral equation on $\partial\Omega s$ derived from Eq. (2.14), is approximated using $\mathbf{d}_1=\mathbf{0}$ as:

$$\phi^S = (\mathbf{I}_N - \mathbf{A}_1)^{-1}\cdot(\mathbf{B}_1\cdot\mathbf{Bt}^S + \mathbf{c}_1), \tag{3.1}$$

where $\mathbf{I}_N$ is a unit matrix $\in \mathbf{R}^{N\times N}$. According to Eq. (3.1), ϕ^S on $\partial\Omega s$ is calculated using $\mathbf{Bt}^S$ on $\partial\Omega s$.

Calculation 2: Input [ϕ^S on $\partial\Omega s$] $\rightarrow$ Output [$\mathbf{Bt}^P$ and ϕ^P on $\partial\Omega_P$].

Equations (2.25) and (2.26), the discretized equations of the boundary integral equations on $\partial\Omega s$ and $\partial\Omega_P$ derived from Eq. (2.16), are approximated using $\mathbf{d}_2=\mathbf{0}$ and $\mathbf{d}_3=\mathbf{0}$ as:

$$\phi^P = ({}^t\mathbf{F}\cdot\mathbf{F})^{-1}\cdot{}^t\mathbf{F}\cdot(\phi^S + \mathbf{B}_2\cdot\mathbf{B}_3^{-1}\mathbf{c}_3 - \mathbf{c}_2), \tag{3.2}$$

$$\mathbf{F} \equiv \mathbf{A}_2 + \mathbf{B}_2\cdot\mathbf{B}_3^{-1}(\mathbf{I}_M - \mathbf{A}_3), \tag{3.3}$$

$$\mathbf{Bt}^P = \mathbf{B}_3^{-1}(\mathbf{I}_M - \mathbf{A}_3)\cdot\phi^P - \mathbf{B}_3^{-1}\mathbf{c}_3. \tag{3.4}$$

where $\mathbf{I}_M$ is a unit matrix $\in \mathbf{R}^{M\times M}$. According to Eqs. (3.2)~(3.4), $\mathbf{Bt}^P$ and ϕ^P on $\partial\Omega_P$ are calculated using ϕ^S on $\partial\Omega_S$. The boundary $\partial\Omega_P$ is presumed to be completely enclosed by the plasma.

Calculation 3: Input [$\mathbf{Bt}^P$ and ϕ^P on $\partial\Omega_P$] $\rightarrow$ Output [ϕ in $\Omega_{B\text{-}P}$].

The flux function values ϕ at any point in the region $\Omega_{B\text{-}P}$ can be obtained by using the following discretized equation of Eq. (2.16). The contour having the highest (or lowest) flux value in a vacuum around a plasma shows the outermost flux surface of a plasma. Thus:

$$\phi(\mathbf{x}) = \zeta_1(\mathbf{x}, \partial\Omega_P)\cdot\phi^P + \zeta_2(\mathbf{x}, \partial\Omega_P)\cdot\mathbf{Bt}^P + \zeta_3(\mathbf{x})\cdot\mathbf{Ic}, \tag{3.5}$$

where $\mathbf{x}$ is an arbitrary observation point in the region $\Omega_{B\text{-}P}$, $\zeta_1(\mathbf{x}, \partial\Omega_P)$ and $\zeta_2(\mathbf{x}, \partial\Omega_P)$ are the vectors resulting from the discretization of the first term in the right hand side of Eq. (2.16), $\mathbf{Ic}$ is the current vector of coils or conductors in the region $\Omega_{B\text{-}P}$, and $\zeta_3(\mathbf{x})$ is the coefficient vector that connects $\mathbf{Ic}$ with the flux value at the point $\mathbf{x}$.

Equation (3.5) shows that once $\partial\Omega_P$ is determined, the coefficient vectors depend on only $\mathbf{x}$. By preparing those vectors in tabular form, the flux function value $\phi(\mathbf{x})$ can be calculated using only the measurements of $\mathbf{Ic}$ and either $\mathbf{Bt}^S$ or ϕ^S. This implies that this method is applicable to real-time control and visualization.

To execute these three outlined calculations, several techniques peculiar to the numerical computation needed by this method are required as discussed in the following portion of this section.

(2) Discretization of the closed curved surfaces

The integral formulas should be converted into finite series for numerical computation. The closed curved surfaces of $\partial\Omega_S$ and $\partial\Omega_P$ are approximated as polygons whose sides must be sufficiently short on the poloidal cross section. For example, for application to JT-60U or ITER, an inscribed 1000-sided polygon is adopted in place of the concerned closed curved surface. The method of division is that (a) the closed surface is redefined as a function $\rho(\theta)$ in polar coordinates whose center is that of the vacuum vessel, (b) the closed curved surface $\rho(\theta)$ is divided into 1000 equal parts of $[\theta_1, \theta_2]$, $[\theta_2, \theta_3]$,... $[\theta_{999}, \theta_{1000}]$, $[\theta_{1000}, \theta_1]$ and (c) a 1000-sided polygon is formed whose vertexes are the points of $(\theta_1,\rho(\theta_1))$, $(\theta_2,\rho(\theta_2))$,... $(\theta_{1000},\rho(\theta_{1000}))$.

The sensors on the closed surface are moved to the nearest middle points of the 1000 sides of the polygon for numerical calculation. The sensors are located at irregular intervals as in actual tokamaks. For this reason, the line

integral along the closed surface requires two types of calculation steps; interpolations and numerical integrations with the regular intervals adjusted by the interpolation. B-spline for a periodic function[12] is applied to the interpolation. The angles in polar coordinates mentioned above are commonly taken as a variable in both interpolations and integrations.

(3) Integral of the interval including a singular point

The integrands of $G(\mathbf{x},\mathbf{y})$ and grad $G(\mathbf{x},\mathbf{y})$ have a singular point of $\mathbf{y}=\mathbf{x}$, but they are integrable in the sense of the Riemannian integral concept. Two methods can be considered: (a) A side having a singular point is discretized. This singular point is the middle point of a certain side of the polygon. By dividing the side into an odd-number of parts of the same length, discretized points are obtained without divergence of the integrands. Using these points, simple numerical integration along this side of the polygon is executed. (b) The integral interval is limited to the neighborhood of the singular point and the analytical integral calculation is performed, as discussed in Appendix 2.

The method (a), the Simpson integral with 19 discretized parts, is found to give adequate accuracy, which will be shown in the following section.

4. Application to JT-60 Upgrade and ITER

The method based on boundary integral equations ("the BIE method") is applied to tokamaks of JT-60 Upgrade (JT-60U) and ITER, and its performance is evaluated in this section. The method of evaluation is as follows: (a) A test plasma is produced by a reliable equilibrium code, and magnetic flux intensities at sensor locations are calculated beforehand. (b) A shape is reproduced by the BIE method using magnetic flux intensities. (c) The identified shape and the flux contour figure produced by the equilibrium code are plotted on the same axis for comparison.

The application of the BIE method to the JT-60U high-β_p divertor plasmas having different current profiles is shown in Fig. 4.1. The closed curved surface for sensors, $\partial\Omega s$, is the vessel wall. Fifty B_t sensors (that measure a component of magnetic field tangential to $\partial\Omega s$) were located along $\partial\Omega s$ at the same interval with respect to angle θ in polar coordinates. The same ellipse:

$$[R_H(\theta), Z_H(\theta)] = [3.33+0.5\cdot\cos\theta \text{ m}, 1.0\cdot\sin\theta \text{ m}],$$

in cylindrical coordinates, was used as the hypothetical plasma surface $\partial\Omega_P$ for all identifications shown in Fig. 4.1. The number of discretized points independent of each other on $\partial\Omega_P$ was 25. These were located at the same

interval with respect to the parameter θ. Figure 4.1 illustrates that differences in plasma current profiles have little influence on the accuracy of identification.

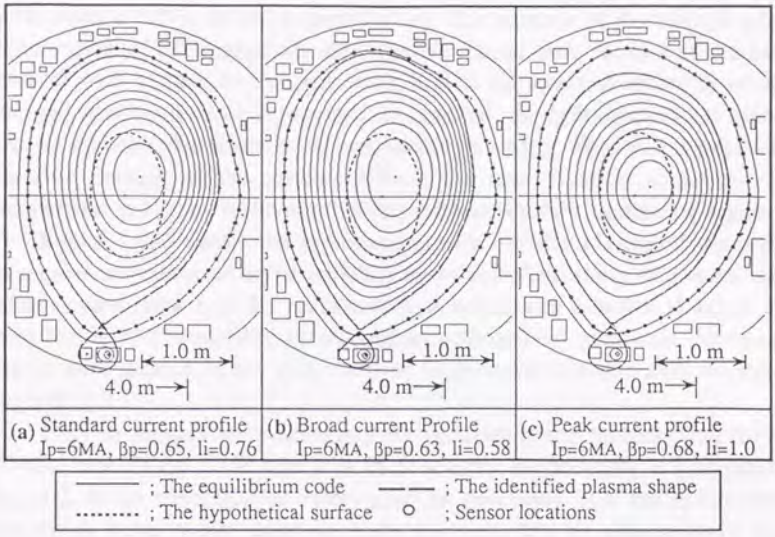

Fig. 4.1 Application to JT-60U High-βp Plasmas with Different Current Profiles

The application of the BIE method to ITER is shown in Fig. 4.2. The identification of the standard high-β_p double-null divertor plasma is presented in Fig. 4.2(a). Figures 4.2(b)~(e) show influences caused by the changes in case (a): (b) the influence of the β_p change, (c) that of the hypothetical plasma surface $\partial\Omega_P$, (d) that of the sensor-plasma distance, and (e) that of noise, where 1% noise[*] was applied to all the magnetic sensors (B_t) and coil current signals. Forty-eight B_t sensors were located symmetrically to the "midplane" (a mirror surface plane for the symmetry, that is often the equatorial plane of a torus) along $\partial\Omega_s$ at the same interval with respect to the parameter θ. The curved surface $\partial\Omega_s$ is defined on the poloidal cross section in cylindrical coordinates as:

$$[R_s(\theta), Z_s(\theta)] = [6.0+a\cdot\cos(\theta+\{\sin^{-1}(0.4)\cdot\sin\theta\})\ \mathrm{m},\ a\cdot\kappa\cdot\sin\theta\ \mathrm{m}].$$

[*]; Random noise which obeys the normal distribution whose standard deviation is 1% of the real value.

The parameters of a and κ are as follows: a=2.3 m and κ=2.2 in (a), (b), (c) and (e), a=2.9 m and κ=2.2 in (d), and a=2.4 m and κ=2.4 in (f). The same ellipse:

$$[R_H(\theta), Z_H(\theta)] = [6.0+1.0\cdot\cos\theta \text{ m}, 2.0\cdot\sin\theta \text{ m}],$$

in cylindrical coordinates, was used for $\partial\Omega_P$ in (a), (b), (d) and (e), and a circle with a 1.5-m radius is used for (c). The number of discretized points independent of each other on $\partial\Omega_P$ was 20. These were located at the same interval with respect to the parameter θ. The influence of either β_P or $\partial\Omega_P$ change was found to be very small. In contrast, the influence of the sensor-plasma distance was found to be comparatively strong. This would imply that the line density of the sensors affects the identification accuracy. The comparison in Fig. 4.2(e) shows that this method is robust against 1% noise.

Figure 4.2(f) shows the reproduction of a circular plasma. Twenty-four Bt sensors were located asymmetrically to the midplane along $\partial\Omega_S$ at the same interval with respect to the parameter θ. A circle with a radius of 1.0 m was used for $\partial\Omega_P$. The number of independent discretized points on $\partial\Omega_P$ was 8 These were located at the same interval in polar coordinates with respect to angle θ.

Fifty Bt sensors were necessary for accurate shape reproduction for the JT-60U case. In the ITER case with 48 Bt sensors, the accuracy is illustrated in Fig. 4.2. If the identification errors must be decreased or if the environment has strong noise and/or unknown eddy currents, then an appropriately large number of sensors are needed. The sensor locations should also be properly determined. At this point, the BIE method can be a useful tool to give a logical determination of sensor locations according to the following logic: The identification errors are produced mainly in the interpolation process. Therefore, if the flux intensity between a pair of adjacent Bt sensors is precisely reproduced using a given interpolation function, the error is minimized. On the other hand, if flux intensity is not precisely reproduced, one or more additional sensors are needed between the adjacent sensors. This is in agreement with a natural conviction that many sensors are needed in an area having strong nonlinearity.

The BIE method gives an accurate ITER identification. While the methods of "filament-current-approximation (FCA)" and "Legendre-Fourier expansion (LFE)" include large identification errors, as mentioned in Section 1, they both give good results for JT-60U applications. What is the real cause of accuracy deterioration? Current sources in FCA and eigenfunctions in LFE are used to reproduce the flux field in a vacuum. Consequently, they determine

both the flux distribution and the flux intensity distribution simultaneously with the determination of one unknown current value in FCA or with that of one unknown coefficient value in LFE. Such limitations should be compensated by increasing the number of either current sources in FCA or eigenfunctions in LFE. However, FCA has difficulty in positioning filament currents, and LFE has difficulty in the numerical computation of higher modes of eigenfunctions. These difficulties posed by FCA and LFE seem to degrade the accuracy for the identification of an ITER plasma with $\kappa \approx 2.2$. As the portion of higher modes is small in the JT-60U case ($\kappa \approx 1.5$), several filament current sources in FCA, or several lower modes of eigenfunctions in LFE, are enough to reproduce the vacuum magnetic field.

In contrast, in the BIE method, flux and flux intensity on the inner boundary $\partial\Omega_P$ are independent variables in the boundary integral equations. They both are determined so that the identified vacuum magnetic field can agree with the magnetic measurements. Therefore, this method has a wider range of freedom than FCA or LFE. It should be understood that this is the reason why the BIE method can identify an ITER plasma much more accurately than FCA and LFE using the same number of sensors.

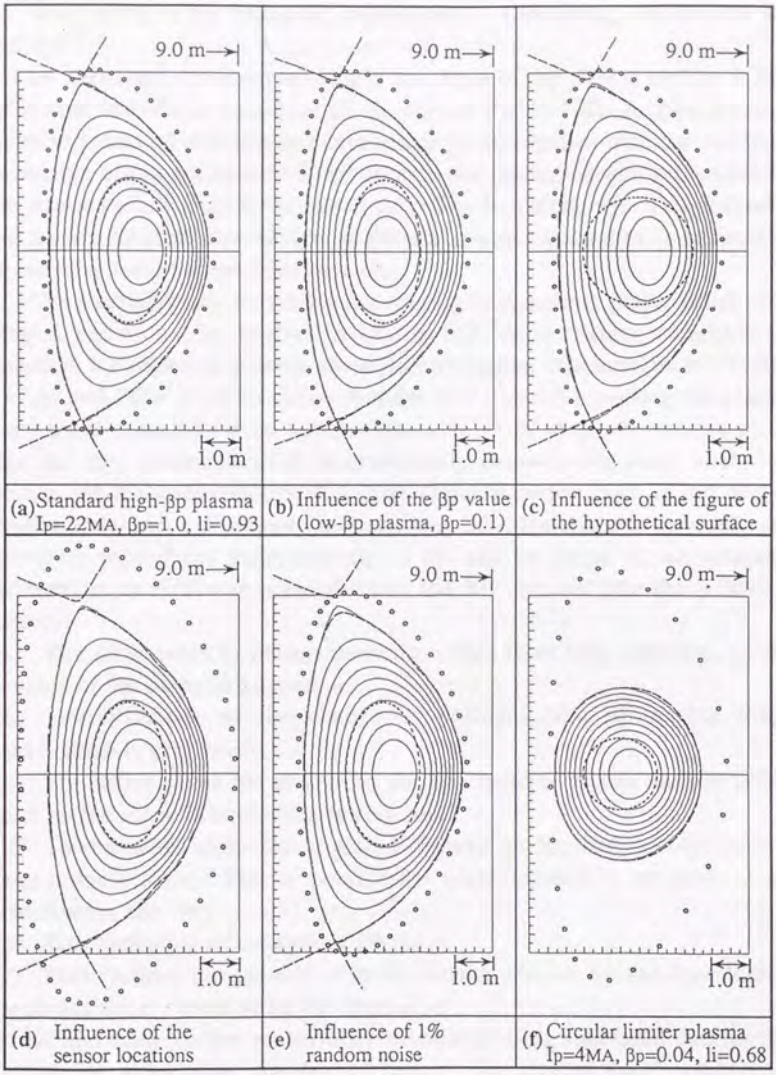

Fig. 4.2 Application to ITER Plasmas

5. Conclusions

As a result of the foregoing discussions, the following conclusions are reached.

A necessary condition to identify the shape of the plasma surface is that either flux intensities tangential to the curved surface $\partial\Omega s$ or flux function values at points on $\partial\Omega s$ can be continuously given together with the complete knowledge of current density distribution in the region, except in the plasma. The sensor surface, $\partial\Omega s$, is the closed curved surface along which the magnetic sensors are located. Knowledge of plasma internal quantities is essentially unnecessary for the shape identification.

The method based on the boundary integral equations (BIE), which uses integral equations for derivation of the defined necessary condition, is proposed for tokamak plasma shape identification. Application to JT-60U ($\kappa \approx 1.5$) and ITER ($\kappa \approx 2.2$) shows that the BIE method identifies the plasma shape more accurately even with a finite number of magnetic sensors along $\partial\Omega s$. As this method is used to numerically compute the exact analytical solution of the concerned partial differential equation, and if the proper number of sensors are properly located along $\partial\Omega s$, the shape is definitely and accurately reproduced independently of the size or shape of the tokamak. Furthermore, several test calculations by the BIE method give the following features:

(a) The differences in plasma current profiles have little influence on the accuracy of the shape identification.

(b) The influence of the change of poloidal beta β_P on the shape identification is very small.

(c) The influence of the change in the hypothetical plasma surface ($\partial\Omega_P$) figure on the shape identification is very small.

(d) The influence of the sensor-plasma distance on the shape identification is comparatively strong. This is because the sensor density is sensitive to the identification accuracy.

(e) This method is robust against 1% noise.

(f) This method can identify a small circular plasma by the hypothetical plasma surface enclosed within the plasma.

As the line integrals are numerically calculated using measured data in this method, an appropriate number of sensors are needed for interpolation. However, the total number of sensors will never be impractical because only a component of the flux intensity vector tangential to $\partial\Omega s$ is necessary.

References in Chapter II.2

[1] Braams, B.J., Plasma Physics and Controlled Fusion, Vol.33 (1991) p.715.

[2] Swain, D.W., Neilson, G.H., Nuclear Fusion, Vol.22 (1982) p.1015.

[3] Kurihara, K., "Improvement of the tokamak plasma shape identification with a Legendre-Fourier expansion of the vacuum poloidal flux function," Fusion Technology, Vol.21, No.11 (1992).

[4] Aikawa, H., et al., Japanese Journal of Applied Physics, Vol.15 (1976) p.2031.

[5] For example;
Kuznetsov, Y.K., et al., Soviet Journal of Plasma Physics, Vol.13 (1987) p.75.
LAO, L.L., et al., "Equilibrium analysis of current profiles in tokamaks," General Atomics Report No. GA-A19668 (1989).

[6] Wesley, J., et al., The ITER poloidal field system, in Plasma Physics and Controlled Nuclear Fusion Research 1990 (IAEA-CN-53/F-III-16, Proc. 13th Int. Conf., Washington D.C., 1990), Vol.3, IAEA, Vienna, (1991) p.421.

[7] Hakkarainen, S.P., Lecture on "MHD and Related Topics in Alcator C-mod" held at Japan Atomic Energy Research Institute (JAERI) (1989).

[8] Morse, P.M., Feshbach, H., "Methods of the Theoretical Physics: Part I," McGraw-Hill Book Company, Inc., New York (1953) p.706.

[9] Brebbia, C.A., Dominguez, J., "Boundary Elements," McGraw-Hill Book Company, Inc., New York (1989) p.51.

[10] Kurihara, K., "Eddy current effect study on JT-60 plasma equilibrium control," Fusion Engineering and Design, Vol.19 (1992) pp.235-257.

[11] Yoshida, K., "Integral Equations," Iwanami Shoten, Tokyo (1950) p.136 (in Japanese).

[12] De Boor, C., "A Practical Guide to Spline," Springer-Verlag, New York (1978).

[13] Azumi, M., et al., "Japanese contribution to ITER PF system design during CDA," JAERI Report No. JAERI-M92-041 (1992).

[14] Hart, J.F., et al., "Computer Approximations," John Wiley & Sons, Inc., New York (1968) p.150.

Appendix 1. Solutions of the PDE for plasma shape identification.

From a mathematical point of view, the problem of identifying the plasma outermost magnetic surface is a type of boundary value problem of an elliptic second-order PDE. In general, there are three well known methods of solving a PDE:

(a) The method of separation of variables

(b) The variational method

----> Finite element method (numerical computation)

(c) The method of boundary integral equations (Green function method)

----> Boundary element method (numerical computation)

All these methods originate from analytical and strict solutions of a PDE. In reality, the solution is numerically computed in either a finite series or at discretized points. The features of these methods and their applicability to shape identification are discussed below.

The method of separation of variables is based on the fact that variables in the Laplace operator (Laplacian, Δ) are separable in Descartes coordinates. Therefore, any set of variables resulting from conformal mapping of Descartes coordinates are separable for the Laplacian. A PDE is converted to multiple ODEs (ordinary differential equations) corresponding to the number of variables in the coordinates being conformal to the Descartes coordinates. The concerned operator in Eq. (2.6), i.e. rot·rot= grad·div - Δ, is separable, though it is not identical with the Laplacian. The basic functions, "eigenfunctions," for Eq. (2.6) in Descartes, cylindrical, toroidal, and spherical coordinates are known. The solution of Eq. (2.6) is then composed of an infinite-series of the eigenfunctions, whose linear coefficients are determined by the boundary condition. It is, however, impossible to determine an infinite number of coefficients from the boundary condition values, which are usually given at discretized finite points. Therefore, a large error may be included, especially in numerical calculations of higher modes of eigenfunctions[3]. This implies that unless the first several series of eigenfunctions can approximate the solution precisely, the calculation will contain a fairly large margin of error. In fact, the Legendre-Fourier expansion method identifies the shapes of low-κ($<$1.8) plasmas very well. However, a plasma with high-κ($\approx$2.2) in ITER is inaccurately reproduced[13]. Thus, the method of separation of variables is not easily applicable to shape identification of highly-elongated plasmas.

The finite element method applied to the whole region including the plasma is known for current profile identification. However, this premises a

fixed outermost plasma surface. Hence the method of weighted residuals is applied to Eq. (2.3) for a vacuum region surrounding the plasma. The current density is $\mathbf{j}=0$, then:

$$\text{rot rot } \mathbf{A} = \mathbf{0}. \tag{A1.1}$$

The vector potential $\mathbf{A}$ is adopted for a weight function. After both sides of Eq. (A1.1) are multiplied by $\mathbf{A}$, the volume integral of both sides over region $\Omega_{S\text{-}P}$ yields:

$$\int_{\Omega S\text{-}P} \mathbf{A}\cdot\text{rot rot } \mathbf{A}\, dV = \int_{\Omega S\text{-}P} (\text{rot } \mathbf{A})^2\, dV - \int_{\partial\Omega S+\partial\Omega P} \mathbf{A}\cdot(\text{rot } \mathbf{A}\times d\mathbf{S}) = 0 \quad , \tag{A1.2}$$

where $\partial\Omega_S$ and $\partial\Omega_P$ are the sensor surface and hypothetical plasma surface, respectively, and $\Omega_{S\text{-}P}$ is the region bounded by both $\partial\Omega_S$ and $\partial\Omega_P$, as shown in Fig. 2.2. Equation (A1.2) is discretized on the finite elements over the region $\Omega_{S\text{-}P}$ and is solved numerically. The boundary value $\mathbf{A}$ on the surfaces $\partial\Omega_S$ and $\partial\Omega_P$ is required for solving Eq. (A1.2). The value of $\mathbf{A}$ on $\partial\Omega_P$, however, cannot be fixed beforehand. Consequently, this approach encounters difficulty when applied to an unfixed boundary value problem.

The method of boundary integral equations is based on a strict formula of the solution of a PDE using a Green function with both Dirichlet and Neumann boundary conditions. Part of the boundary shape and value cannot be fixed, being the same as the situation previously mentioned. However, the following features exist in the boundary integral equation method: (1) The Dirichlet and Neumann conditions on the surface $\partial\Omega_S$ can be derived from each other by putting the boundary $\partial\Omega_B$ (enclosing the analytical region) analytically and infinitely far from the concerned region (see Fig. 2.2). (2) The Dirichlet and Neumann conditions on $\partial\Omega_P$ can be computed using those conditions on $\partial\Omega_S$. The feature (1) is "an infinitely far boundary," which is one of the difficulties of numerical computation. The feature (2) implies that flux function extrapolation toward the plasma is possible. Furthermore, no difficulty arises in numerical computation of the solution expressed as a complete formula because a boundary integral with singularity is stable. As the hypothetical plasma boundary $\partial\Omega_P$ must be located sufficiently inside a plasma, it is necessary to roughly know the plasma shape prior to identification. ∎

Appendix 2. Infinite-series formula of the line integral along the interval including a singular point.

It is well known that a definite integral of a continuous regular function can be expressed as an infinite-series formula. If the integrand with a singular point diverges to infinity, and if the definite integral is bounded in the sense of the Riemannian integral, can the integral result be expressed as an infinite-series formula? The answer will be discussed within this appendix.

Singular integrals introduced for boundary integral equations are

$$S_{G\nabla\phi} \equiv \int_{\partial\Omega_i} G(x, y)\cdot \mathrm{grad}\phi(y)\cdot \frac{dS(y)}{r_y^2} \quad , \text{(A2.1)} \qquad S_{\phi\nabla G} \equiv \int_{\partial\Omega_i} \phi(y)\cdot \mathrm{grad}G(x, y)\cdot \frac{dS(y)}{r_y^2} \quad , \text{(A2.2)}$$

where $\partial\Omega_i$ is a closed surface including a singular point on the poloidal cross section.

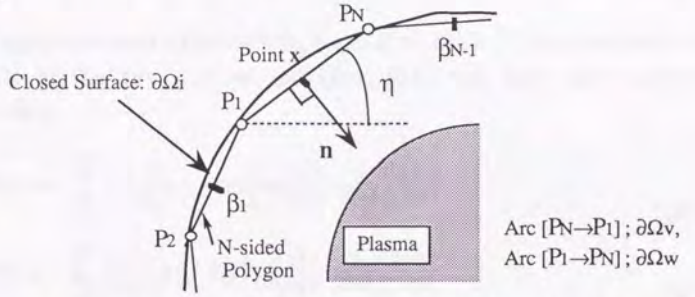

Fig. A2.1 N-sided Polygonal Approximation of the Closed Surface and the Definitions of Points and a Vector

Now $\partial\Omega_i$ is divided into two regions; a sufficiently small region involving a singular point ($\partial\Omega v$) where the flux function is presumed to be constant, and the region of the remainder ($\partial\Omega w$), i.e. $\partial\Omega_i = \partial\Omega v + \partial\Omega w$. The integral over $\partial\Omega w$ is a normal integral and can be expressed as an infinite series. The closed surface $\partial\Omega_i$ is approximated by the polygon in the same manner as in Section 2, and is shown in Fig. A2.1. The singular point **x** is presumed to be the middle point of the side $P_N P_1$, whose length is $2\cdot h$. This side $P_N P_1$ is taken as $\partial\Omega v$. This region is sufficiently small such that $S_{G\nabla\phi}$ and $S_{\phi\nabla G}$ are approximated as:

$$\int_{\partial\Omega V} G(x, y)\cdot \mathrm{grad}\phi(y)\cdot \frac{dS(y)}{r_y^2} \approx \mathrm{grad}\phi(x)\cdot \int_{-h}^{h} G(x, y)\cdot \mathbf{n}\, \frac{2\pi\, ds}{r_y} \quad , \qquad \text{(A2.3)}$$

$$\int_{\partial\Omega_V} \phi(y)\cdot \mathrm{gradG}(x,y)\cdot \frac{dS(y)}{r_y^2} \approx \phi(x)\cdot \int_{-h}^{h} \mathrm{gradG}(x,y)\cdot \mathbf{n}\, \frac{2\pi\, ds}{r_y} \quad , \tag{A2.4}$$

where the variable s in the integrands is a distance along the side P_NP_1 from the middle point $\mathbf{x}$ whose position vector is $\mathbf{x}\equiv(r_x,z_x)$, $\mathbf{y}\equiv(r_y,z_y)$, $r_y=r_x+s\cdot\cos\eta$, $z_y=z_x+s\cdot\sin\eta$, $\mathbf{n}$ is a vector inward normal to the side P_NP_1, as shown in Fig. A2.1 and the slope of the side is $\tan\eta$. The right hand sides of Eqs. (A2.3) and (A2.4) are rewritten. Thus:

$$\int_{-h}^{h} G(x,y)\cdot\mathbf{n}\, \frac{2\pi\, ds}{r_y} = 8\pi \begin{pmatrix} \sin\eta \\ -\cos\eta \end{pmatrix} \int_0^h K(k)\, ds - 16\pi \begin{pmatrix} \sin\eta \\ -\cos\eta \end{pmatrix} \int_0^h E(k)\, ds \quad , \tag{A2.5}$$

$$\int_{-h}^{h} \mathrm{gradG}(x,y)\cdot\mathbf{n}\, \frac{2\pi\, ds}{r_y} = \frac{4\pi\sin\eta}{r_x} \int_0^h K(k)\, ds - \frac{8\pi\sin^3\eta}{r_x} \int_0^h E(k)\, ds \quad . \tag{A2.6}$$

Using approximations of $k\approx 1-s^2/(8r_x^2)$ and $k^2\approx 1-s^2/(4r_x^2)$, the complete elliptic integrals of the first and second kind, K(k) and E(k), are analytically integrated as:

$$\int_0^h K(k)\, ds = \sum_{i=0}^{10} \left(\frac{1}{8r_x^2}\right)^i \left[p_{Ki} - q_{Ki}\cdot\left\{ \log\left(\frac{h^2}{8r_x^2}\right) - \frac{2}{2i+1} \right\} \right] \frac{h^{2i+1}}{2i+1} \quad , \tag{A2.7}$$

$$\int_0^h E(k)\, ds = \sum_{i=0}^{10} \left(\frac{1}{8r_x^2}\right)^i \left[p_{Ei} - q_{Ei}\cdot\left\{ \log\left(\frac{h^2}{8r_x^2}\right) - \frac{2}{2i+1} \right\} \right] \frac{h^{2i+1}}{2i+1} \quad , \tag{A2.8}$$

where p_{Ki}, q_{Ki}, p_{Ei} and q_{Ei} are constant coefficients that were prepared for calculations of K(k) and E(k) with double precision (i.e. 8 bytes=1 word)[14].

As a result of the derivations above, both Eqs. (A2.1) and (A2.2) are understood to have the same formula at $\mathbf{x}=\alpha$:

$$\int_{\partial\Omega_i} H(\alpha,\beta)\cdot q(\beta)\, d\beta = \int_{\partial\Omega_W} H(\alpha,\beta)\cdot q(\beta)\, d\beta + \int_{\partial\Omega_V} H(\alpha,\beta)\cdot q(\beta)\, d\beta \quad , \tag{A2.9}$$

$$\approx \sum_{i=1}^{N-1} w(h_i,\alpha,\beta_i)\cdot q(\beta_i) + Y(h,\alpha)\cdot q(\alpha) \quad , \tag{A2.10}$$

where the first and second terms in Eq. (A2.9) corresponds to those in Eq. (A2.10). The bounded function $Y(h,\alpha)$ is easily derived from Eqs. (A2.5)~(A2.8). By using the following definitions in the second term of Eq. (A2.10):

$$\beta_N \equiv \alpha,\ h_N \equiv h \text{ and } w(h_N,\alpha,\alpha) \equiv Y(h,\alpha),$$

the right hand side of Eq. (A2.10) results in:

$$\sum_{i=1}^{N} w(h_i, \alpha, \beta_i) \cdot q(\beta_i)$$

Increasing N to infinity, Eq. (2.17) is obtained:

$$\int_{\partial\Omega_i} H(\alpha, \beta) \cdot q(\beta)\, d\beta = \sum_{i=1}^{\infty} w(h_i, \alpha, \beta_i) \cdot q(\beta_i) \qquad \text{(A2.11)}$$

In actual calculation, Eq. (A2.10) is used instead of Eq. (A2.11). The integral interval $\partial\Omega v$ should be determined to be small enough to regard ϕ as a constant in $\partial\Omega v$, while the integrand must not overflow numerically in the integral interval $\partial\Omega w$. ∎

Appendix 3. The result of the BIE method gives an exact solution for a vacuum region with the hypothetical plasma surface located inside the plasma.

Shape identification based on boundary integral equations (the BIE method) requires the hypothetical plasma surface to be located inside the plasma. The definitions are repeated as follows: $\partial\Omega_P$ is the hypothetical plasma surface completely enclosed by the plasma, $\partial\Omega_{P^*}$ is the real plasma surface, and $\partial\Omega_S$ is the surface along which the magnetic sensors are located. The solution of Eq. (2.4) with taking $\partial\Omega_P$ is defined as $\xi(\mathbf{x})$, and can be expressed as:

$$\sigma\cdot\xi(\mathbf{x}) = \int_{\partial\Omega_P} [G\cdot\mathrm{grad}\phi - \phi\cdot\mathrm{grad}G]\cdot\frac{dS(y)}{r_y^2} + \int_{\Omega_{P\text{-}\infty}} \mu_0(j_c+j_v)\cdot G\cdot\frac{dV(y)}{r_y} \quad , \tag{A3.1}$$

where the vector S is normal to the surface in the direction toward the plasma, j_c and j_v are the known current densities in the regions $\Omega_{S\text{-}\infty}$ and $\Omega_{P\text{-}S}$, respectively, and $\sigma \equiv \{8\pi^2\ (\Omega_{P\text{-}\infty}\supset\mathbf{x}),\ 4\pi^2\ (\partial\Omega_P\supset\mathbf{x}),\ 0\ ((\text{exterior to } \Omega_{P\text{-}\infty})\supset\mathbf{x})\}$. On the contrary, by assuming the plasma current density j_p is known, the solution $\phi(\mathbf{x})$ is given by:

$$\sigma\cdot\xi(\mathbf{x}) = \int_{\partial\Omega_P} [G\cdot\mathrm{grad}\phi - \phi\cdot\mathrm{grad}G]\cdot\frac{dS(y)}{r_y^2} + \int_{\Omega_{P\text{-}\infty}} \mu_0(j_c+j_v+j_p)\cdot G\cdot\frac{dV(y)}{r_y} \quad . \tag{A3.2}$$

By introducing the surface $\partial\Omega_{P^*}$, Eq. (A3.2) can be rewritten as:

$$\sigma\cdot\phi(\mathbf{x}) = \sigma^{\#}\cdot\psi(\mathbf{x}) + \int_{\partial\Omega_{P^*}} [G\cdot\mathrm{grad}\phi - \phi\cdot\mathrm{grad}G]\cdot\frac{dS(y)}{r_y^2} + \int_{\Omega_{P^*\text{-}\infty}} \mu_0(j_c+j_v)\cdot G\cdot\frac{dV(y)}{r_y} \quad , \tag{A3.3}$$

where $\sigma^{\#}\cdot\psi(\mathbf{x})$ is defined as:

$$\sigma^{\#}\cdot\psi(\mathbf{x}) \equiv \int_{\partial\Omega_P} [G\cdot\mathrm{grad}\phi - \phi\cdot\mathrm{grad}G]\cdot\frac{dS(y)}{r_y^2} - \int_{\partial\Omega_{P^*}} [G\cdot\mathrm{grad}\phi - \phi\cdot\mathrm{grad}G]\cdot\frac{dS(y)}{r_y^2} + \int_{\Omega_{P^*\text{-}P}} \mu_0 j_p\cdot G\cdot\frac{dV(y)}{r_y} \quad , \tag{A3.4}$$

and $\sigma^{\#} \equiv \{8\pi^2\ (\Omega_{P^*\text{-}P}\supset\mathbf{x}),\ 4\pi^2\ ((\partial\Omega_{P^*} \text{ or } \partial\Omega_P)\supset\mathbf{x}),\ 0\ ((\text{exterior to } \Omega_{P^*\text{-}P})\supset\mathbf{x})\}$. In a vacuum region (exterior to $\Omega_{P^*\text{-}P}$), $\sigma^{\#}\cdot\psi(\mathbf{x})=0$ in Eq. (A3.3). Consequently, Eq. (A3.3), in which the plasma current density is taken into account, is expressed for a vacuum region as:

$$\sigma\cdot\phi(\mathbf{x}) = \int_{\partial\Omega_{P^*}} [G\cdot\mathrm{grad}\phi - \phi\cdot\mathrm{grad}G]\cdot\frac{dS(y)}{r_y^2} + \int_{\Omega_{P^*-\infty}} \mu_0(j_c+j_v)\cdot G\cdot\frac{dV(y)}{r_y} \quad . \tag{A3.5}$$

On the other hand, by introducing the plasma surface $\partial\Omega_{P^*}$ in Eq. (A3.1), then:

$$\sigma\cdot\xi(\mathbf{x}) = \int_{\partial\Omega_P} [G\cdot\mathrm{grad}\phi - \phi\cdot\mathrm{grad}G]\cdot\frac{dS(y)}{r_y^2} - \int_{\partial\Omega_{P^*}} [G\cdot\mathrm{grad}\phi - \phi\cdot\mathrm{grad}G]\cdot\frac{dS(y)}{r_y^2}$$
$$+ \int_{\partial\Omega_{P^*}} [G\cdot\mathrm{grad}\phi - \phi\cdot\mathrm{grad}G]\cdot\frac{dS(y)}{r_y^2} + \int_{\Omega_{P-\infty}} \mu_0(j_c+j_v)\cdot G\cdot\frac{dV(y)}{r_y} \quad . \tag{A3.6}$$

The summation of the first and second terms in Eq. (A3.6) is a nonzero value only inside the region Ω_{P^*-P}, and it vanishes in a vacuum, as is the same derivation with $\sigma^{\#}\cdot\psi(\mathbf{x})$ in Eqs. (A3.3) and (A3.4). Taking into account that there is no current flow in Ω_{P^*-P}, then:

$$\sigma\cdot\xi(\mathbf{x}) = \int_{\partial\Omega_{P^*}} [G\cdot\mathrm{grad}\phi - \phi\cdot\mathrm{grad}G]\cdot\frac{dS(y)}{r_y^2} + \int_{\Omega_{P^*-\infty}} \mu_0(j_c+j_v)\cdot G\cdot\frac{dV(y)}{r_y} \quad . \tag{A3.7}$$

The right hand side of Eq. (A3.7) is identical with that of Eq. (A3.5). Finally:

$$\phi(\mathbf{x}) = \xi(\mathbf{x}). \tag{A3.8}$$

Therefore, it is understood that with the hypothetical plasma surface located inside the plasma, the result from the BIE method gives an exact solution for a vacuum region. ∎

Chapter III

Dynamics of Plasma Equilibrium Control

A tokamak plasma is a very light conductor carrying high current with high magnetic field from the view point of equilibrium control. Consequently, zero inertia approximation is valid in the time scale of the poloidal field (PF) coil current control by the digital computer. As force balance is always preserved inside and outside the plasma column, "dynamics" results from the magnetic field propagation of the PF coils and the magnetic field induced by the plasma motion. A vacuum vessel and other conductors of structural components make the problem more complicated. Plasma-vessel-PF-coils are electromagnetically interacting with each other, and these resultant field determines the plasma motion. As feedback control should be applied to the system, control algorithms should be involved in the dynamical model. In this chapter, the analytical method based on the classical electromagnetic theory is introduced to decompose those interactions.

In Chapter III.1, the $\mathbf{A}$-ϕ method ($\mathbf{A}$ is the magnetic vector potential and ϕ is the scalar potential) was applied to eddy current analysis in the JT-60 tokamak fusion device. This analysis agrees with the coil excitation experiments much better than the filament-current-coil approximation does with them. The accuracy of the $\mathbf{A}$-ϕ method is estimated by comparing it with the analytical solution of magnetic field penetration into an infinitely long cylindrical conductor. A JT-60 plasma equilibrium-control-dynamics (ECD) model including eddy currents induced in the vacuum vessel is proposed for control system design and analysis. Considering the plasma-vessel interaction, the one-point plasma model and its equilibrium force balance are assumed. Comparison of the simulation and experimental data identifies the essential points for reproduction of the plasma ECD: (a) Magnetic field induced by the plasma motion is proportional to its velocity. (b) Magnetic field penetration is regarded as a response of a first-order differential equation. Application limits of the employed model are also identified: (a) Plasma volume effects are not accurately involved. (b) Influence of eddy current on shape evolution is not taken into consideration.

As a result of the analysis in Chapter III.1, the A-ϕ method is understood to be effective. Then, in Chapter III.2, the synthetic numerical model of equilibrium control dynamics based on the A-ϕ method is built up. The finite element formulation is completed. Necessary tools for the analysis such as automatic mesh generator, algebra for large-scale sparse matrices, etc., are also newly developed.

III.1 Eddy Current Effect Study on the JT-60 Plasma Equilibrium Control

1. Introduction

Tokamak plasma experiments are eagerly supported because of their promise to reach the breakeven condition needed for thermonuclear fusion reactors. One important and necessary aspect in these experiments is plasma equilibrium control. This control may well determine the possible operating regimes and thus is related directly to achievable plasma performance. A plasma itself can always be assumed to follow an external electromagnetic field preserving its inner equilibrium. The external field is produced by controlled poloidal field (PF) coil currents and uncontrolled/undetectable eddy currents induced by both PF coils and plasma motion. Eddy currents, consequently, play an essential role in the transient phenomenon of equilibrium. Among the many design studies on tokamak equilibrium control reported to date, some studies considered eddy current effects; others neglected the existence of eddy currents. Eddy current analyses for the design of electromagnetic industrial products such as motors, computer disk read/write heads and a wide assortment of transducers, etc., have advanced in conjunction with recent theoretical investigations of analysis and the rapid development of computer performance. The A-ϕ method (A is the magnetic vector potential and ϕ is the scalar potential), one of the three-dimensional eddy current analyses based on Maxwell's quasi-steady-state (qss) equations, is selected for JT-60 tokamak application because the governed equations are derived exactly from Maxwell's qss equations without any approximation. (Several previous methods that approximated conductors as filament-current-coils (FCCs) have been applied to tokamaks.) In this study a calculation based on the A-ϕ method is compared with the exact analytical solution of Maxwell's qss equations in an infinitely long cylindrical conductor geometry. Also studies in tokamak geometry are the calculations of the poloidal magnetic field ($\mathbf{B}_P$) penetration into the vacuum vessel using three methods; the A-ϕ method, the FCC approximation and the infinitely-thin-plate (ITP) approximation. In Section 2, these methods are also compared with the experimental results of JT-60 PF coil excitation tests (performed without a plasma). The calculations show that $\mathbf{B}_P$ penetration can be modelled as a system of a first-order differential equation having a time constant fixed at the observation point. It will be shown that this makes the model much simpler. In addition to $\mathbf{B}_P$ penetration, the magnetic fields created by eddy currents induced by the plasma movement, the voltage-current

relation for the PF coils, the flux consumption, the plasma motion and the control system are also discussed for modelling of plasma equilibrium control. The simulations and JT-60 experiments are compared in the control of JT-60 vertical and horizontal plasma displacements within and beyond $0<n_{index}<1.5$ in Section 3. The method used to establish the control model from the design parameters is discussed in Section 4. The limitation of reproducibility and errors in this model are presented, and problems in the FCC approximation for the vacuum vessel are also described in Section 4.

2. Poloidal Field Penetration into the Vacuum Vessel

2.1 Overview of the Eddy Current Analyses: the A-ϕ method and others

Several methods to reproduce a transient eddy current phenomenon have been proposed for design engineering and data analysis of industrial products, accelerators, fusion devices, etc. The benchmark tests are performed where common models are computed by several methods and the results are compared with each other as well as with experimental data[1]. In this study, three methods for calculations in tokamak geometry are selected; the **A**-ϕ method, the infinitely-thin-plate (ITP, or shell) approximation[2] (a particular case of the **T** method[3]) and the filament-current-coil (FCC) approximation[4]. The **A**-ϕ method is based on Maxwell's quasi-steady-state (qss) equations;

$$\mathrm{rot}\ \mathbf{H} = \mathbf{j}, \tag{2.1}$$

$$\mathrm{rot}\ \mathbf{E} = -\frac{\partial \mathbf{B}}{\partial t}, \tag{2.2}$$

$$\mathbf{B} = \mu_0 \mathbf{H}, \tag{2.3}$$

$$\mathrm{div}\ \mathbf{B} = 0, \tag{2.4}$$

and Ohm's law;

$$\mathbf{j} = \sigma\, \mathbf{E}.\ (\sigma\ ;\ \text{an electrical conductivity tensor}) \tag{2.5}$$

The introduction of the vector and scalar potentials, **A** (**B**=rot**A**) and ϕ, gives

$$\mathrm{rot\ rot}\ \mathbf{A} = \mu_0 \sigma \cdot \left(-\frac{\partial \mathbf{A}}{\partial t} - \mathrm{grad}\phi \right). \tag{2.6}$$

By taking **A** as a weight function for Eq. (2.6) and integrating over the three-dimensional analytical domain Ω with boundary $\partial\Omega$, we obtain the integral formula of Eq. (2.6);

$$\int_{\Omega} [(\mathrm{rot}\ \mathbf{A})^2 - \mathbf{A} \cdot \mu_0 \cdot \sigma \cdot \left(-\frac{\partial \mathbf{A}}{\partial t} - \mathrm{grad}\phi \right)] dV = \int_{\partial\Omega} \mathbf{A} \cdot (\mathrm{rot}\ \mathbf{A} \times \mathbf{n}) dS, \tag{2.7}$$

where **n** is the vector normal to the boundary surface. A gauge or a condition permissible in gauge transformations provides a necessary scalar equation for **A** and ϕ. Kirchhoff's law,

$$\mathrm{div}\ \mathbf{j}=\mathrm{div}\ \sigma\cdot\left(-\frac{\partial \mathbf{A}}{\partial t}-\mathrm{grad}\phi\right)=0, \tag{2.8}$$

is adopted as the scalar equation in the used **A**-ϕ method. By solving numerically Eqs. (2.7) and (2.8) using discretized finite elements of space and time, the evolution of **A** and ϕ is obtained. This method is based on classical electromagnetic theory[*]. However, different methods, such as the infinitely-thin-plate (ITP) and filament-current-coil (FCC) approximations, have been often used for eddy current analyses of tokamaks.

The ITP (or shell) approximation[2] is a special case of the **T** method[#][3] and the normal component of the current vector potential **T** (**j**=rot **T**) to the conductor plate is used as an unknown variable. The tangential components are neglected in the analysis.

The FCC approximation is a well-known method applied to tokamak fusion devices[4]. In this approximation, many toroidally-looped filament coils are arranged in a group in place of a doughnut-shaped axisymmetric vacuum vessel. This has the advantage that the field evolution at any point can be easily obtained by solving simple circuit equations. The validity of this observation, however, seems never to have been verified theoretically or experimentally in the case of toroidally non-uniform vacuum vessel.

2.2 Calculations of Poloidal Field Penetration into the Vacuum Vessel Compared with JT-60 Experiments

(1) Infinitely long cylinder geometry

The accuracy of the **A**-ϕ method is initially estimated by comparison with the analytical solution of magnetic field penetration into an infinitely long cylindrical conductor. A current of $37.5+2.5\sin(2f\pi t)$ kA & f=5 Hz is forcibly induced in a filament current wire located parallel to the conductor. The dimensions of this geometry are shown in Fig. 2.1. Only a single component (Az) of the vector potential (which is parallel to the filament current) exists as an unknown variable. The Coulomb gauge, div**A**=0 is used for this analysis. The electrical field is produced only in the z-direction. Therefore, no electric

[*]: The **A**-ϕ method presented here adopts Eq. (2.8) instead of a gauge condition. Consequently, ϕ is not able to be determined in a nonconductive region. Therefore, the electric field by grad ϕ, which propagates through the nonconductive region, cannot be taken into account.

[#]: The **T** method is based on Maxwell's qss equations and is similar to the **A**-ϕ method.

charge appears on the cylinder and ϕ can be set to zero (gradϕ=**0**). The following diffusion equation, which governs eddy current behavior in the conductor, is obtained from Eq. (2.6), div**A**=0 and gradϕ=**0**;

$$\Delta Az = \sigma\mu_0 \frac{\partial Az}{\partial t} . \qquad (2.9)$$

The vector potential Az on the outer surface of the conductor is not only a function of filament current but is also a function of the eddy current behavior defined by Eq. (2.9). This makes "a pre-unfixed Dirichlet-boundary value problem of a parabolic partial differential equation." The analytical solution of this equation can be expressed as an infinite-series of the Bessel-Fourier expansion;

$$Az(\rho,\theta,t)=\sum_{\nu=0}^{\infty}\sum_{\lambda=1}^{\infty} C_{\nu\lambda}(t)\cdot J_\nu(\omega_{\nu\lambda}\rho)\cdot\cos\nu\theta + \sum_{\nu=0}^{\infty} D_\nu(t)\cdot\left(\frac{\rho}{a}\right)^\nu\cdot\cos\nu\theta \qquad (2.10)$$

where J_ν is the ν-th order Bessel function of the first kind, $\omega_{\nu\lambda}$ is a constant of separation of variables, a is a radius of the cylinder, (ρ,θ) is polar coordinates, as shown in Fig. 2.1, and $C_{\nu\lambda}(t)$ and $D_\nu(t)$ are coefficients of linear combinations of eigenfunctions. $C_{\nu\lambda}(t)$ and $D_\nu(t)$ are obtained by solving the ν-sets of the $(\lambda+1)$ simultaneous first-order differential equations (see Appendix).

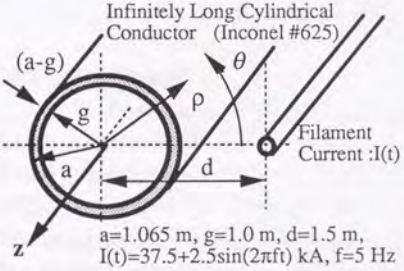

Fig. 2.1 Infinitely Long Cylinder Geometry and (ρ,θ,z) Coordinates

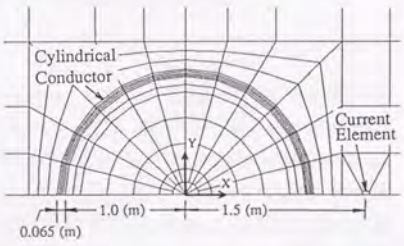

Fig. 2.2 Mesh Division of the Infinitely Long Cylindrical Conductor

To apply the A-ϕ method to this model, the conductor and the remaining region are divided into appropriate small pieces of finite elements. The analytical region is a thin slab bounded by two planes perpendicular to the z-axis. Each plane is a 200 m × 200 m square to avoid the influence of the boundary condition on the conductor area. Figure 2.2 shows a view of the

mesh division from z=∞ over the analytical region. A three-dimensional calculation is performed on this model with the boundary condition being that the magnetic field vector $\mathbf{B} \equiv (B_X, B_Y)$ is perpendicular to the z-axis. The discretized time step is 12.5 msec.

The calculations of B_Y penetration by the **A**-ϕ method and analytical solution for the center of the cylinder are compared in Fig. 2.3. The analytical solution for the center can be obtained by using $\{D1(t), C1_\lambda(t), \lambda=1 \text{ to } 20\}$. It provides the accuracy of the **A**-ϕ method for reproduction of the **B** diffusion behavior; errors of the phase and amplitude at a frequency of 5 Hz are ~5 degrees fast and ~10% less than full amplitude.

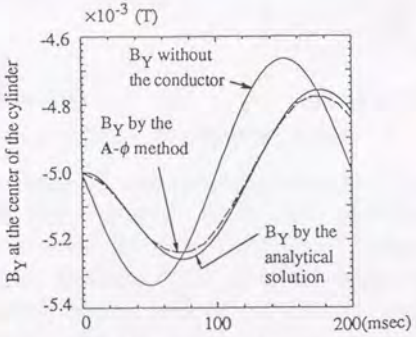

Fig. 2.3 B_Y Time Evolution at the Center of the Cylinder

(2) JT-60 geometry

A vertical field (VF) coil excitation test was performed in the JT-60 fusion experimental device without a plasma, and the VF coil current was varied according to a preset waveform. The vacuum vessel, made from Inconel #625, is formed by joining eight 6.5 cm-thick rigid ring sectors (thick conductor parts) and eight 0.2 cm-thick bellows (bellows parts), alternately in the toroidal direction, as shown in Fig. 2.4(a). The bellows offer high electrical resistance in the toroidal direction and, consequently, lower resistance in the poloidal direction. The toroidally developed length of a bellows is 8.3 times the actual length of the bellows. Magnetic field (**B**) sensors (magnetic probes) are located at six poloidally-different points just inside the thick part of the vacuum vessel wall on the same poloidal plane. These sensors measure the two components of **B** (normal and tangential directions to the

wall). Figure 2.4(b) is a poloidal cross-sectional view of the vessel showing PF coils and sensor locations in a sector.

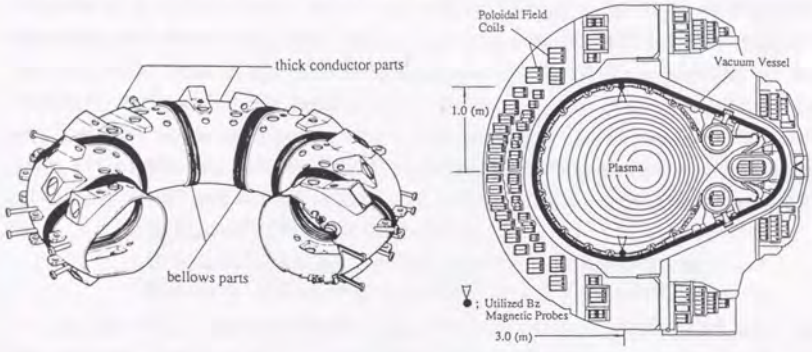

(a) The Cutaway View (b) The Cross-Sectional View

Fig. 2.4 JT-60 Vacuum Vessel

The following methods and data will now be compared; (i) the **A**-ϕ method, (ii) the ITP approximation, (iii) the FCC approximation, and (iv) the experimental data obtained from the VF coil excitation test. In the **A**-ϕ method, the anisotropic electrical conductivity is used to represent the bellows characteristics. A mesh division view of the analytical region of the vacuum vessel is shown in Fig. 2.5. The cylindrical coordinates (R,ω,Z) are now adopted to explain the boundary conditions.

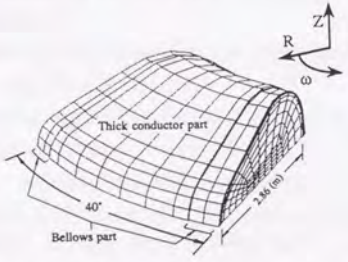

Fig. 2.5 Mesh Division of JT-60 Vacuum Vessel

The analytical region is bounded by four planes and a curved surface; two planes perpendicular to Z-axis, two planes perpendicular ω-axis and a curved surface R=100 m. The different boundary conditions can be independently set on the planes and the surface. The upper boundary of the plane perpendicular

to the Z-axis is extended to 100 m away from the "midplane (the equatorial plane of the torus)." The outboard boundary of the curved surface is also extended to R=100 m away from Z-axis (R=0). These were done so improper boundary conditions would not cause an unfavorable influence on the analysis. The magnetic field **B** on both boundaries is restricted to be parallel to the boundary surfaces whose normal unit vector is **n**, i.e. $\mathbf{B}\cdot\mathbf{n}=0$. **B** should be perpendicular to the midplane on the lower boundary due to the JT-60 up-and-down symmetry, i.e. $\mathbf{B}\times\mathbf{n}=0$. The remaining boundary planes are the sector cut-ends of $\omega=0°$ and $\omega=40°$, where a periodic boundary condition is adopted, i.e.

$$|\mathbf{B}(R,\omega=0°,Z)|=|\mathbf{B}(R,\omega=40°,Z)|,$$
$$\mathbf{B}(R,\omega=0°,Z)\cdot\mathbf{n}(\omega=0°)=\mathbf{B}(R,\omega=40°,Z)\cdot\mathbf{n}(\omega=40°) \text{ and}$$
$$\{\mathbf{B}(R,\omega=0°,Z)\times\mathbf{n}(\omega=0°)\}_Z=\{\mathbf{B}(R,\omega=40°,Z)\times\mathbf{n}(\omega=40°)\}_Z.$$

In the FCC approximation, the vacuum vessel is divided into 84 axisymmetric one-turn coils. Two kinds of loop resistance are considered; one is the actual one-turn electrical resistance and the other is the resistance without the bellows parts. Thus, the bellows effect on the field penetration will be known.

In the ITP approximation, 464 eigenmodes of the finite element circuits are used to represent the eddy current flow patterns[2].

Figures 2.6 and 2.7 show the Bz time evolutions calculated by the **A**-ϕ methods, FCC and ITP approximations together with the sensor signal obtained from the experiment. Figure 2.6 compares the following calculations and data at the sensor location:

(A0) Bz in the experiment (in steady-state oscillation).
(A1) Bz without the vessel.
(A2) FCC approximation (bellows+thick conductor parts).
(A3) **A**-ϕ method in the JT-60 geometry.
(A4) FCC approximation (thick conductor parts only).
(A5) **A**-ϕ method with the vessel composed of only the thick conductor parts.

(A3) shows the best reproduction of the experimental data (A0). Slight deviations of amplitude and phase are observed, though they are within the error of the **A**-ϕ method, as described in Section 2. Conductors neglected in the analysis such as diagnostic access ports and support structures may increase the time constant of the penetration. The penetration speed in (A2) is much faster than the actual (A0) and closer to (A1). On the other hand, the **A**-ϕ method (A5) and the FCC approximation (A4) calculations correlate well in this axisymmetric geometry. This indicates the thick conductor parts seem to determine the time response of the field to the sensor.

Figure 2.7 shows the comparison of Bz time evolution at the center of the vessel for the following calculations:

(B1) Bz without the vessel.

(B2) FCC approximation (bellows+thick conductor parts).

(B3) **A**-ϕ method beneath the bellows.

(B4) FCC approximation (thick conductor parts only).

(B5) **A**-ϕ method beneath the thick conductor part.

(B6) ITP approximation(toroidal average along the central axis of the vessel).

(B3) and (B5) are the results from the **A**-ϕ method calculation, similar to (A3) and (A5). (B3) shows almost no retardation from (B1), while (B5) indicates a peak-to-peak delay of ~12 msec. On the other hand, (B2) shows a few milliseconds delay and (B4) shows extreme retardation of the penetration. The average Bz along the axis in the vessel by the **A**-ϕ method would be slower than (B3) and faster than (B5), but (B6), calculated by the ITP approximation, closely agrees with (B5). Thus, the ITP approximation estimates a slightly slower field penetration than the **A**-ϕ method.

These results can be interpreted as follows:

(1) It appears that the FCC cannot reproduce the VF coil field penetration into the vacuum vessel. However, the FCC approximation agrees with the **A**-ϕ method if the vessel is axisymmetric.

(2) The **A**-ϕ method reproduces well the phenomenon if all the conductors are included in the analytical region.

(3) The time response of the field penetration to the magnetic sensor located on the wall inside the thick part is determined by the time constant of the thick conductor part. In contrast, the response time to the center of the vessel is much less than that to the sensor; it has almost no delay. This implies that the field penetrates the vessel rapidly through the bellows parts and slightly later through the thick conductor parts. Therefore, the response time to the plasma is predominantly determined by the characteristics of the bellows. As a plasma is affected by even a small change in magnetic field, the time constant of the field to the plasma movement is estimated to be less than ~6 msec, half of the discretized time step (12.5 msec).

(4) The ITP approximation shows good reproduction even though eddy current flow across the bellows shell plate is neglected. The field penetration response to the center is determined by the eddy currents in the thin bellows and little current flow across the bellows plate exists. Therefore, the preferable situation seems to make good reproduction calculated by the ITP approximation.

In addition, as the system response of the field evolution at the center of the vessel shows very short delay, a system of a first-order differential equation can be presumed to approximate this system. This simplifies the JT-60 system model.

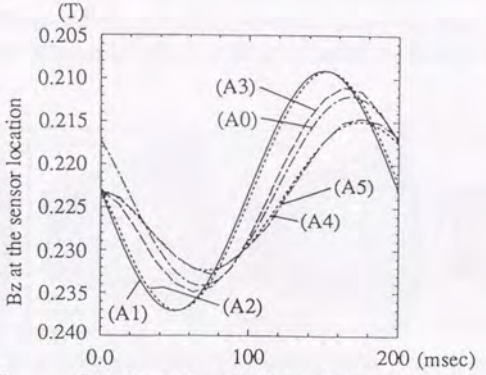

(A0): —·— :Bz in the experiment.(in the steady-state oscillation)
(A1): —— :Bz without the vessel.
(A2): ------- :FCC approximation where one-turn electrical resistances are given by the bellows+thickconductor parts.
(A3): — — :A-ϕ method in the JT-60 geometry.
(A4): ------- :FCC approximation where one-turn electrical resistances are given by the thick conductorparts only.
(A5): — — :A-ϕ method in the geometry where the vessel is composed of only the axisymmetric thick conductor parts.

Fig. 2.6 Bz Time Evolution at the Sensor Location (R=3.0 m, Z=1.0 m)

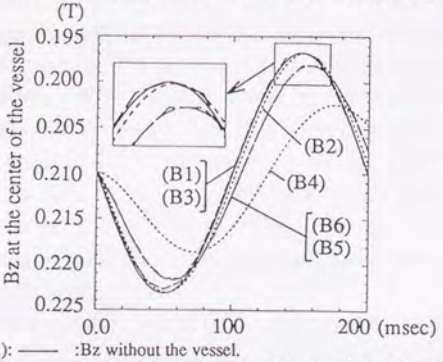

(B1): —— :Bz without the vessel.
(B2): ------- :FCC approximation where one-turn electrical resistances are given by the bellows+thick conductor parts.
(B3): — — :A-ϕ method beneath the bellows.
(B4): ------- :FCC approximation where one-turn electrical resistances are given by the thick conductor parts only.
(B5): — — :A-ϕ method beneath the thick conductor parts.
(B6): —·— :ITP approximation.

Fig. 2.7 Bz Time Evolution at the Center of the Vessel (R=3.0 m, Z=0.0 m)

Figure 2.8 shows the time evolution of eddy current flow in the vessel conductor induced by the vertical field penetration. The major mode is found to be a saddle-shaped-circulating current induced in the thick conductor parts. It would be, of course, more realistic to account for phenomena such as the eddy current flow around the diagnostics-access ports on the thick conductor part. However, the dominant behavior is understood by this simple modelling of the vessel.

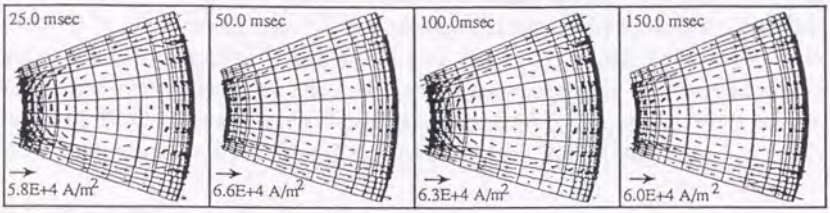

Fig. 2.8 Time Evolution of Eddy Current Flow in the Vessel Conductor Induced by the Vertical Field Penetration
(Eddy currents at t=25 and 50 msec flow in opposite direction to those at t=100 and150 msec, respectively.)

3. JT-60 Plasma ECD Model with Eddy Current Induced in the Vacuum Vessel

The plasma movement should be taken into consideration for design of the ECD (equilibrium-control-dynamics) model. Though the external field propagates through the wall component in the same manner as the no-plasma analysis in the previous section, it behaves in a different way inside the vessel due to the movement of the plasma. Next, phenomena associated with the plasma-vessel interactions will be examined. The penetrated field immediately makes the plasma begin to move according to the $\mathbf{J}\times\mathbf{B}$ force. The plasma weight is negligibly small so acceleration occurs in a very short time period. The plasma tries to accelerate to the Alfvén velocity. However, the plasma cannot move at such a high speed because a retarding force is produced by its movement in the following ways;

(a) the force of the magnetic field that is a function of the plasma location acts on the plasma. If decay index (n_{index}) of the magnetic field at the plasma location is within $0<n_{index}<1.5$, the plasma is positionally stable.
(b) the PF (poloidal-field) coil voltage induced by the plasma movement produces a magnetic field that opposes plasma movement, and
(c) the induced eddy currents in the vacuum vessel also produce a field that opposes plasma movement.

Plasma in a field whose decay index is beyond $0<n_{index}<1.5$ is unstable without wall stabilization. The growth rate of such a plasma depends on the magnetic field strength at the moving plasma location, the induced PF coil current and the eddy current in the vessel. If the growth rate is suppressed to a low level, feedback control of the PF coil current could stabilize the plasma. To date, the study of such dynamics (plasma ECD) has been conducted on stability analyses by considering (the above) phenomena (a) & (b)[5] or on simulation studies by taking (a), (b) & (c) into account, where the eddy current is presumed to be induced in the L (inductance)-R (resistance) circuits of the coils instead of the solid vessel conductor[4]. The validity of the latter model, however, is still unverified experimentally. The L-R circuits approximation is almost identical with the FCC (filament-current-coil) approximation. The applicability of the FCC approximation to JT-60 will be discussed later in this chapter.

3.1 JT-60 Plasma ECD Scheme

Tokamak plasma behavior is known to be a result of the electromagnetics and/or particle interactions with the device components such as the PF coils, the vacuum vessel, the first wall, etc. They would also include the behavior of the control system including power supplies and position calculations for consideration in longer time-scale analysis (more than 1 msec). However, for the model of ECD, it is understood that it is not necessary to involve all the microscopic interactions. This is shown by past experience with tokamak devices. Therefore, only the essential phenomena are included in the JT-60[*] simplified ECD scheme as shown in Fig. 3.1.

The phenomena in Fig. 3.1 are modelled as follows:

(1) Penetration delay of the magnetic field

The magnetic field penetration through the vacuum vessel is governed by a system of a first-order differential equation that has a time constant of τ, as discussed in Section 2. τ_R and τ_Z denote the time constants of the vertical and horizontal field penetration, respectively.

(2) The magnetic field by the plasma axisymmetric movement

This magnetic field is produced by the eddy current, which is induced in the vacuum vessel by the movement of the plasma. The movement is presumed to obey axisymmetric rigid-body motion. Consequently, the magnetic field $\mathbf{B}_{move}$ (T) is assumed to be a two-dimensional column vector$\equiv{}^t(B_R,B_Z)$, where the superscript ^{t} denotes a transposition of the matrix. The production of $\mathbf{B}_{move}$

[*]: JT-60 cross-sectional view is shown in Fig. 2.4(b). The ellipticity κ was able to be changed from less than 0.5 to greater than 1.6 by the quadrupole field (QF) coil.

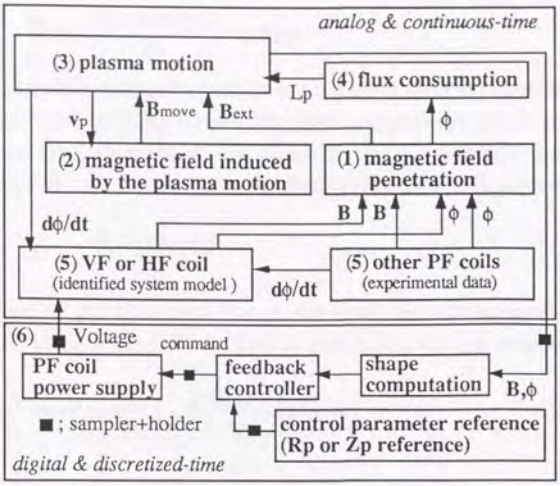

Fig. 3.1 JT-60 Plasma Equilibrium Control Dynamics
(The number in the figure corresponds to the sub-section number in Section 3.1.)

will now be examined in detail. The plasma current is assumed to remain constant. When a plasma column with current I_p (A) axisymmetrically moves as a result of plasma-conductor interactions at a velocity vector $\mathbf{v}_p$ (m/sec) $\equiv {}^t(v_Z, v_R)$, the magnetic field lines of the plasma current must cut the vessel wall at almost the same speed as the plasma if the plasma mass is assumed to be zero. The change of the magnetic field **B** resulting from plasma motion produces an electrical field **E** in the vessel according to the Maxwell's equation;

$$\text{rot } \mathbf{E} = -\frac{\partial \mathbf{B}}{\partial t}. \tag{3.1}$$

Using vector potentials, **B** is expressed as

$$\mathbf{B} = \text{rot } (\mathbf{A}_p + \mathbf{A}_{eddy}), \tag{3.2}$$

where $\mathbf{A}_p$ and $\mathbf{A}_{eddy}$ are the vector potentials produced by the plasma current and eddy current that is induced by the plasma movement, respectively. The plasma current density $\mathbf{j}_p$ and eddy current density $\mathbf{j}_{eddy}$ satisfy Maxwell's qss equations as follows;

$$\text{rot rot } \mathbf{A}_p = \mu_0 \mathbf{j}_p, \tag{3.3}$$
$$\text{rot rot } \mathbf{A}_{eddy} = \mu_0 \mathbf{j}_{eddy}. \tag{3.4}$$

A scalar potential ϕ is introduced to express **E** explicitly, then

$$\mathbf{E} = -\frac{\partial(\mathbf{A}p+\mathbf{A}eddy)}{\partial t} - \mathrm{grad}\phi \qquad (3.5)$$

Now the plasma axisymmetric motion in an axisymmetric vessel is considered. The electrical field resulting from such plasma motion is produced only in the toroidal direction. Therefore, no electric charge appears on the vessel conductor and ϕ can be set to zero, $\phi=0$ ($\mathrm{grad}\phi=\mathbf{0}$). Equation (3.5) then becomes

$$\mathbf{E} = -\frac{\partial(\mathbf{A}p+\mathbf{A}eddy)}{\partial t} \qquad (3.6)$$

The imposition of the Coulomb gauge, $\mathrm{div}\mathbf{A}_p=0$ and $\mathrm{div}\mathbf{A}_{eddy}=0$, allows Eqs. (3.3) and (3.4) to be solved. Then $\mathbf{A}_p(\mathbf{r},t)$ and $\mathbf{A}_{eddy}(\mathbf{r},t)$ are obtained;

$$\mathbf{A}_p(\mathbf{r},t)=\frac{\mu_0}{4\pi}\int_{\Omega p}\frac{\mathbf{j}_p(\mathbf{s}(t),t)}{|\mathbf{r}-\mathbf{s}(t)|}dV(\mathbf{s}(t)) \qquad (3.7)$$

$$\mathbf{A}_{eddy}(\mathbf{r},t)=\frac{\mu_0}{4\pi}\int_{\Omega v}\frac{\mathbf{j}_{eddy}(\mathbf{s},t)}{|\mathbf{r}-\mathbf{s}|}dV(\mathbf{s}) \qquad (3.8)$$

where Ωp is the total region occupied by a plasma and Ωv is a conductor in which an eddy current is induced by the movement of the plasma; and $\int\cdot dV(\mathbf{s})$ denotes the volume integral with respect to the position vector variable $\mathbf{s}$. According to Ohm's law,

$$\mathbf{j}_{eddy}(\mathbf{s},t)=\sigma(\mathbf{s})\cdot\mathbf{E}(\mathbf{s},t)= -\sigma(\mathbf{s})\cdot\partial(\mathbf{A}_p(\mathbf{s},t)+\mathbf{A}_{eddy}(\mathbf{s},t))/\partial t, \qquad (3.9)$$

where $\sigma(\mathbf{s})$ is an $\mathbf{R}^{3\times3}$ electrical conductivity tensor. Substituting Eq. (3.9) for the right hand side of Eq. (3.8) , we obtain

$$\mathbf{A}_{eddy}(\mathbf{r},t)= -\frac{\mu_0}{4\pi}\int_{\Omega v}\frac{\sigma(\mathbf{s})}{|\mathbf{r}-\mathbf{s}|}\cdot\frac{\partial\left(\mathbf{A}_p(\mathbf{s},t)+\mathbf{A}_{eddy}(\mathbf{s},t)\right)}{\partial t}dV(\mathbf{s}) \qquad (3.10)$$

Furthermore, the repeated substitutions of Eq. (3.10) for $\mathbf{A}_{eddy}$ in the right hand side of Eq. (3.10) give the infinite series formula of $\mathbf{A}_{eddy}$;

$$\mathbf{A}_{eddy}(\mathbf{r},t) = -\frac{\mu_0}{4\pi}\frac{\partial}{\partial t}\left[\int_{\Omega v}\frac{\sigma(\mathbf{s})\cdot\mathbf{A}_p(\mathbf{s},t)}{|\mathbf{r}-\mathbf{s}|}dV(\mathbf{s})\right]$$
$$+\sum_{n=2}^{\infty}\left(-\frac{\mu_0}{4\pi}\frac{\partial}{\partial t}\right)^n\left[\int_{\Omega v}\cdots\int_{\Omega v}\frac{\{\sigma(\mathbf{s}_1)\sigma(\mathbf{s}_2)\cdots\sigma(\mathbf{s}_n)\}\cdot\mathbf{A}_p(\mathbf{s}_1,t)}{|(\mathbf{r}-\mathbf{s}_n)\cdot(\mathbf{s}_n-\mathbf{s}_{n-1})\cdots(\mathbf{s}_2-\mathbf{s}_1)|}dV(\mathbf{s}_1)dV(\mathbf{s}_2)\cdots dV(\mathbf{s}_n)\right], \qquad (3.11)$$

where $\{s_i, i=1,2,...,n\}$ is a position vector for each integral operation. For JT-60, the scalar conductivity σ of Inconel #625 is $7.69\times10^5\,\Omega^{-1}m^{-1}$ and $(\sigma\mu_0/4\pi)^n \sim(0.0769)^n$. The higher time derivatives of the vector potential, $(\partial/\partial t)^n \mathbf{A}_p(\mathbf{s}_1,t)$, become smaller than the time derivatives of the lower ones in the time scale being considered. Therefore, only the first term of Eq. (3.11) can adequately provide an accurate approximation of $\mathbf{A}_{eddy}$. Now the first term of Eq. (3.11) is calculated. The time derivative of Eq. (3.7) yields the formula for $\partial \mathbf{A}_p(\mathbf{r},t)/\partial t$;

$$-\frac{\partial \mathbf{A}_p(\mathbf{r},t)}{\partial t} = \left[-\frac{\mu_0}{4\pi}\int_{\Omega p} \left\langle \frac{\partial}{\partial \mathbf{s}} \left(\frac{\mathbf{j}_p(\mathbf{s})}{|\mathbf{r}-\mathbf{s}|} \right) \right\rangle dV(\mathbf{s}) \right] \cdot \mathbf{v}_p(t) \tag{3.12}$$

$$\equiv \mathbf{F}(\mathbf{r})\cdot\mathbf{v}_p(t). \tag{3.13}$$

In the above derivation, the plasma current density $\mathbf{j}_p$ on the plasma boundary $\partial\Omega p$ is set to 0 and the plasma is assumed to move like a rigid-body. $\mathbf{F}(\mathbf{r})$ is an $\mathbf{R}^{3\times2}$ matrix. The bracket $\langle\ \rangle$ is defined as follows;

$$\left\langle \frac{\partial}{\partial \mathbf{s}} \left(\frac{\mathbf{j}_p(\mathbf{s})}{|\mathbf{r}-\mathbf{s}|} \right) \right\rangle \equiv \left[\frac{\partial}{\partial R}\left(\frac{\mathbf{j}_p(\mathbf{s})}{|\mathbf{r}-\mathbf{s}|} \right) \quad \frac{\partial}{\partial Z}\left(\frac{\mathbf{j}_p(\mathbf{s})}{|\mathbf{r}-\mathbf{s}|} \right) \right] \in \mathbf{R}^{3\times2} . \tag{3.14}$$

$\mathbf{A}_{eddy}(\mathbf{r},t)$ is obtained by substituting Eq. (3.12) for the first term of Eq. (3.11);

$$\mathbf{A}_{eddy}(\mathbf{r},t) \approx \frac{\mu_0}{4\pi}\left[\int_{\Omega v} \frac{\sigma(\mathbf{s})\cdot\mathbf{F}(\mathbf{s})}{|\mathbf{r}-\mathbf{s}|} dV(\mathbf{s}) \right] \cdot \mathbf{v}_p(t) . \tag{3.15}$$

The magnetic field $\mathbf{B}_{move}$ produced by $\mathbf{j}_{eddy}(\mathbf{r},t)$ is given by

$$\mathbf{B}_{move}(\mathbf{r},t) = \mathrm{rot}\ \mathbf{A}_{eddy}(\mathbf{r},t), \tag{3.16}$$

and by applying the rotation operator on Eq. (3.15),

$$\mathbf{B}_{move}(\mathbf{r},t) = \frac{\mu_0}{4\pi}\left[\int_{\Omega v} \frac{[\{\sigma(\mathbf{s})\cdot\mathbf{F}(\mathbf{s})\}\#(\mathbf{r}-\mathbf{s})]}{|\mathbf{r}-\mathbf{s}|^\beta} dV(\mathbf{s}) \right] \cdot \mathbf{v}_p(t) \tag{3.17}$$

$$\equiv \mathbf{H}(\mathbf{r})\cdot\mathbf{v}_p(t). \tag{3.18}$$

The operator # is defined as follows;

$$[\mathbf{M}\#\mathbf{u}] \equiv \left[\begin{pmatrix} {}^t\mathbf{m}_\alpha \\ {}^t\mathbf{m}_\beta \\ {}^t\mathbf{m}_\gamma \end{pmatrix} \# \begin{pmatrix} u_\alpha \\ u_\beta \\ u_\gamma \end{pmatrix} \right] \equiv \begin{bmatrix} {}^t\mathbf{m}_\beta\cdot u_\gamma - {}^t\mathbf{m}_\gamma\cdot u_\beta \\ {}^t\mathbf{m}_\gamma\cdot u_\alpha - {}^t\mathbf{m}_\alpha\cdot u_\gamma \\ {}^t\mathbf{m}_\alpha\cdot u_\beta - {}^t\mathbf{m}_\beta\cdot u_\alpha \end{bmatrix} \in \mathbf{R}^{3\times k} \tag{3.19}$$

where $\mathbf{M} \in \mathbf{R}^{3\times k}$, $\mathbf{m}_i \in \mathbf{R}^{k\times 1}$ and $\mathbf{u}_i \in \mathbf{R}^{3\times 1}$. In this case plasma movement is presumed to be two-dimensional, therefore, k=2. Strictly speaking, the $\mathbf{R}^{3\times 2}$ matrix function $\mathbf{H}(\mathbf{r})$ depends on the distribution of plasma current density. $\mathbf{H}(\mathbf{r})$ can be normalized by I_p, $\mathbf{H}(\mathbf{r}) = \gamma(\mathbf{r}) \cdot I_p$. By considering only the axisymmetric motion of the plasma, and assuming uniform $\mathbf{B}_{move}$ and invariant current distribution, the following simplified approximate expression is obtained.

$$\mathbf{B}_{move} = \mathbf{K} \cdot \mathbf{v}_p \cdot I_p, \tag{3.20}$$

where $\mathbf{K}$ (T/(A·m/sec)) is a coefficient matrix, which is now assumed as a diagonal constant matrix$\equiv$diag$(k_R, k_Z) \in \mathbf{R}^{2\times 2}$. The elements of this matrix are related to the electrical conductivity of vessel materials and locations of conductors to the plasma and the volumes of the conductors. It must be stressed that Eq. (3.20) implies the induced magnetic field is generated instantly by the plasma motion and is proportional to the velocity of the plasma.

(3) Plasma motion

Plasma macroscopic motion is governed by Newton's equation for a rigid body;

$$m_p \cdot d\mathbf{v}_p/dt = \mathbf{F}_{total}, \tag{3.21}$$

where m_p is the mass of the plasma and $\mathbf{F}_{total}$ is the total force vector applied to the plasma column. We can assume $m_p \cdot d\mathbf{v}_p/dt \approx \mathbf{0}$ for a macroscopic motion in a time scale of a millisecond. In other words, it maintains the balance of the total force; $\mathbf{F}_{total} \approx \mathbf{0}$. $\mathbf{F}_{total}$ is then given by

$$\mathbf{F}_{total} \equiv \int_{\Omega_p} \left(\text{grad } p - \mathbf{j}_p \times \mathbf{B}\right) dV$$
$$\approx \mathbf{F}_p - 2\pi R_p I_p \{\mathbf{B}_{ext}(R_p, Z_p) + \mathbf{B}_{move}\} \approx 0, \tag{3.22}$$

where p and $\mathbf{B}$ are plasma pressure and a magnetic field vector in the plasma column, respectively; $\mathbf{B}_{ext}$ is a magnetic field vector generated by the PF coils, which is a function of the macroscopic plasma position (R_p, Z_p); R_p, Z_p and a_p are the major radius, vertical displacement and minor radius, respectively. $\mathbf{F}_p$ is plasma internal force, i.e.,

$$(\mathbf{F}_p)_R \equiv \kappa^{-\alpha}(1/2)\mu_0 I_p^2 \{\log(8R_p/a_p) + (\beta_p + l_i/2) - 3/2\} \text{ [6,7] and} \tag{3.23}$$
$$(\mathbf{F}_p)_Z \equiv 0, \tag{3.24}$$

where $\beta_p + l_i/2$ is the lambda parameter; and $\kappa^{-\alpha}$ is the volume effect (κ is plasma ellipticity, $\alpha \sim 1/4$[7]). Now Eq. (3.23) is rewritten using the plasma self-inductance $L_p \equiv \mu_0 R_p \{\log(8R_p/a_p) + l_i/2 - 2\}$ and

$$(\mathbf{F}p)_R \equiv \kappa^{-\alpha}\{(1/2)Ip^2Lp/Rp+(1/2)\mu_0Ip^2(\beta p+1/2)\}, \quad (3.25)$$

is obtained. Lp in this formula is closely related to the flux consumption.

(4) Flux consumption

Flux conservation is adequate when considering positional instability during a short period, but the flux consumption should be examined for the long-period (>1 second) reproduction of the plasma ECD. The equilibrium of the supply and consumption of flux is expressed as

$$[\phi^{PF}(t) + \phi^{OH}(t)] - [LpIp + \int \eta pIpdt + \phi^{eddy}(t)] = 0, \quad (3.26)$$

where the former and latter brackets show the supply and consumption of flux, respectively, $\phi^{PF}(t)$ and $\phi^{OH}(t)$ are the time-integrated fluxes produced by the PF coils except the ohmic-heating (OH) coil and by the OH coil only, respectively, $\phi^{eddy}(t)$ is the flux consumed by eddy currents in the structural materials and $\int \eta pIpdt$ is the flux consumed by the plasma electrical resistance. Equation (3.26) is assumed to hold at the start of the simulation($t=t_0$). In addition, the following are assumed during the simulation. (a) $\Delta(\theta\cdot\phi^{OH} - \int \eta pIpdt - \phi^{eddy}(t))=0$, where Δ denotes the deviation from the value at $t=t_0$ and θ is the ratio of the OH coil flux consumed by the plasma and conductors. (b) The other PF coil fluxes are neither consumed by the plasma and conductors in the structure. Then by applying Δ to Eq. (3.26), the simple expression;

$$\Delta\phi^{PF} + (1-\theta)\cdot\Delta\phi^{OH} - \Delta(Lp\cdot Ip) = 0, \quad (3.27)$$

is obtained. This equation is used to substitute Lp in Eq. (3.27) for that in Eq. (3.25).

(5) PF coils

JT-60 has five types of PF coils; ohmic heating (OH) coil, vertical field (VF) coil, horizontal field (HF) coil, quadrupole field (QF) coil and divertor (D) coil. The VF and HF coils are the only actuators which control plasma horizontal and vertical displacement. The waveforms same with the experimental data are used for the currents of OH, QF, D and (VF or HF) coils in the simulation. Models of the VF and HF coils will now be developed using the system identification method that uses data of the PF coil impedance measurements. The models are presumed to have the form;

$$\boldsymbol{L}\ (I_{coil}/V_{coil}) = \sum C_i / (1+s\cdot T_i), \quad (3.28)$$

where $\boldsymbol{L}$ (I_{coil}/V_{coil}) is the Laplace transform of the ratio I_{coil}/V_{coil}, I_{coil} is the coil current, V_{coil} is the coil voltage, T_i is the i-th time constant, C_i is the i-th coefficient and s is the parameter in the Laplace transform space ($s=2\pi f \cdot j$, f is frequency, $j=\sqrt{-1}$). The integer ratio of the designed time constant of the coils is taken as T_i. Then the linear coefficient C_i is selected by the least-squares method so that Eq. (3.28) can fit the figures observed on Bode diagrams. The electrical circuit equivalent to the resultant Eq. (3.28) is solved in the ECD simulation, where V_{coil} and I_{coil} are the input and output, respectively.

The inductive couplings between the OH/QF/D coils and the VF/HF coils are included in the model. But the couplings from the VF coil to the OH/QF/D coils and from HF coil to the OH/QF/D coils are neglected in this model because currents of the OH/QF/D coils are well controlled by JT-60 power supplies.

The mutual coupling to the PF coils by the plasma movement is considered. At the start of plasma motion this coupling produces voltage in a coil and the coil current starts to change according to the time constant of the coil (not instantly). The field produced by the current change of PF coils acts to restore the plasma displacement. Consequently, if only this field is taken as $\mathbf{B}_{move}$ in Eq. (3.22), it is impossible to determine v_p using the assumption of $m_p \cdot dv_p/dt=0$. However, it is possible to estimate v_p (or the growth rate) by solving Newton's equation Eq. (3.21) (see Section 4). Such v_p would be more severe than really exists and, therefore, depending on the circumstances, that value might be effective in the initial phase of tokamak design.

(6) Control system (including the PF coil power supply)

The importance of modelling the control system dynamics seems to be little understood to date, but it is an essential task for the construction of ECD system. The discretization (sampler & holder), digitization, dead time and control elements, all essential characteristics of the control system, are completely reproduced in the model. In the control elements, proportional and differential control algorithm is executed every 1 msec in the JT-60 plasma control system together with minimal-time and other control methods in the PF coil power supply controller[8]. The actual control voltages are applied to the coils by thyrister convertors.

The unknown parameters in the simplified model are now summarized:

(1) Penetration delay of the magnetic field

τ_R (sec) ; time constant of the vertical field.

τ_Z (sec) ; time constant of the horizontal field.

(2) Magnetic field induced by the plasma axisymmetric movement

k_R (T/(A·m/sec)) ; conversion constant of the radial motion.

k_Z (T/(A·m/sec)) ; conversion constant of the vertical motion.

(3) Plasma motion:

α ; the power of $\kappa^{-\alpha}$ (the volume effect) in Eq. (3.23).

(4) Flux consumption:

θ ; the OH coil flux consumed by the plasma and conductors.

(5) PF coils and (6) Control system do not contain any unknown parameter.

3.2 Determination of the Unknown Parameters in the ECD Model

Though the unknown parameters of τ_R, τ_Z, k_R, k_Z, α and θ are expected to be predetermined by only the knowledge of the design parameters of the device, an accurate simulation code including the plasma internal behavior will be required to obtain their precise values. Now determination of these values will be undertaken using the JT-60 experimental data. The aim is to identify the simplest ECD model that can reproduce the essentials of the plasma movement. The method to predetermine the parameters will be discussed in the next section.

The simulation was performed under the following conditions;

(a) the control reference waveforms of Rp or Zp are identical with experimental data,

(b) the waveforms of the other coils' currents, which are not directly related to the Rp and Zp control, are also identical with the experimental data and

(c) no parameters except τ_R, τ_Z, k_R, k_Z, α and θ exist to adjust the ECD model.

In the Rp damping oscillation experiment, where the QF coil current was abruptly changed so as to change κ of the plasma from 1.0 to 0.6,

(d) α was adjusted so that the amplitude in the ECD simulation agrees with that in the experiment, ---> $\alpha = 0.132 \sim 1/7$

(e) θ was adjusted so that Bz evolution in the ECD simulation agrees with that in the experiment, ---> $\theta = 0.7$

(f) τ_R was adjusted so that the damping rate of the amplitude in the ECD simulation agrees with that in the experiment and ---> $\tau_R = 4.1$ msec

(g) k_R was adjusted so that the period of oscillation in the ECD simulation agrees with that in the experiment. ---> $k_R = 1.6\times10^{-9}$ T/(A·m/sec)

===> The parameters for the Rp control characteristics are fixed from the Rp damping oscillation experiment.

In the Zp step response experiment,

(h) τ_Z was adjusted so that the damping rate of the amplitude after the overshoot in the ECD simulation agrees with that in the experiment and
---> τ_Z = 2.5 msec

(i) k_Z was adjusted so that the period of oscillation in the ECD simulation agrees with that in the experiment. ---> $k_Z = 1.3\times10^{-9}$ T/(A·m/sec)

===> The parameters for the Zp control characteristics are fixed from the Zp step response experiment.

Thus, all the unknown parameters in the ECD model are determined through the comparison of the data from the simulation and experiment. It must be noted that this small number of adjusting parameters are adequate for the reproduction of JT-60 plasma ECD. Figures 3.2(a) and 3.2(e) show comparisons of the adjusted-model-based simulations and the experiments on control of Rp and Zp, used for the parameter evaluation, together with the magnetic field Bz and BR at the plasma position, respectively.

3.3 Several Simulations Using the ECD Model

The fixed model should be confirmed to reproduce plasma ECD in several other cases. The selected simulation shots, in which the plasma positions were changed, and their main parameters are shown in Table 3.1.

Figure 3.2(b) shows good agreement of Rp ramp response. The sawtoothed waveform of Bz is well reproduced. It may be caused by the time-discretized reference produced by the sampler & holder shown in Fig. 3.1. This is an unavoidable aspect of the digital control system. Figure 3.2(c) shows slow Rp outboard displacement, where a coarse digit of the coil current is observed in Bz waveform. A 10 Hz Rp oscillation experiment is shown in Fig. 3.2(d). The error in the simulation is 4 mm of the amplitude. A sawtoothed waveform of Bz similar to that in Fig. 3.2(b) was observed.

Figure 3.2(f) shows Zp downward step response in the same discharge as shown in Fig. 3.2(e). Good agreement between the simulation evolution and experimental result is recognized. In Fig. 3.2(g), Zp was moved upward with feedback control just as the plasmas were being elongated from 1.0 to 1.4. In Fig. 3.2(h), Zp was moved downward with feedback control just as the plasmas were being elongated from 1.0 to 1.2. As κ became larger, the fluctuation of the horizontal magnetic field BR increased in amplitude as shown in both Fig. 3.2(g) and 3.2(h) (slightly). Differences between the simulation and experiment in the BR evolution are caused by the volume effect of plasmas. It is noteworthy that a BR of only one Gauss(=1.0×10^{-4} T) is sufficient to cause a Zp movement speed of 0.1 m/sec with a 700 kA plasma in JT-60.

Table 3.1 Main Parameters of the Discharge Pulses Used in the Simulation

Shot No.	Ip MA	Divertor/ Limiter	βp+li/2	κ	Rp reference m	Zp reference m	Fig. 3.2
E4244	0.5	Lim.	0.6	1.0(t=0.7sec)→ 0.6(t=0.73sec)	Rp=3.11	Zp=0.0	(a)
E4969	2.3	Div.	0.6	1.0	Rp=3.08(t=4.0sec) →3.045(t=4.1sec)	Zp=0.0	(b)
E5716	1.0	Lim.	0.8	1.0	Rp=3.02(t=3.0sec) →3.08(t=4.0sec)	Zp=0.0	(c)
E5524	1.0	Div.	0.8	1.0	Rp=3.11+0.01sin(20πt) t>3.0sec, 10 Hz	Zp=0.0	(d)
E3622	1.5	Lim.	0.8	1.0	Rp=3.02	Zp=0.0(t=2.5sec)→0.05(t=2.6sec) Zp=0.05(t=7.0sec)→0.0(t=7.1sec)	(e)&(f)
E4557	0.7	Lim.	1.0	1.0(t=1.5sec)→ 1.4(t=3.0sec)	Rp=3.02	Zp=0.0(t=1.5sec)→0.15(t=3.0sec)	(g)
E4559	0.7	Lim	1.0	1.0(t=1.5sec)→ 1.2(t=3.0sec)	Rp=3.02	Zp=0.0(t=1.5sec)→ - 0.15(t=3.0sec)	(h)

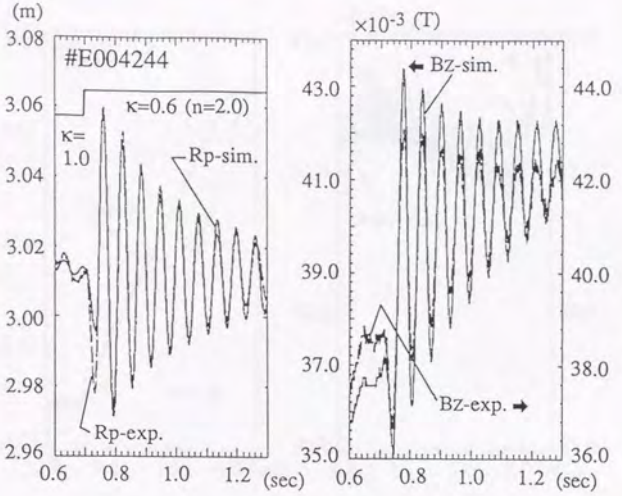

(a) Rp damping oscillation induced by the step change of κ.

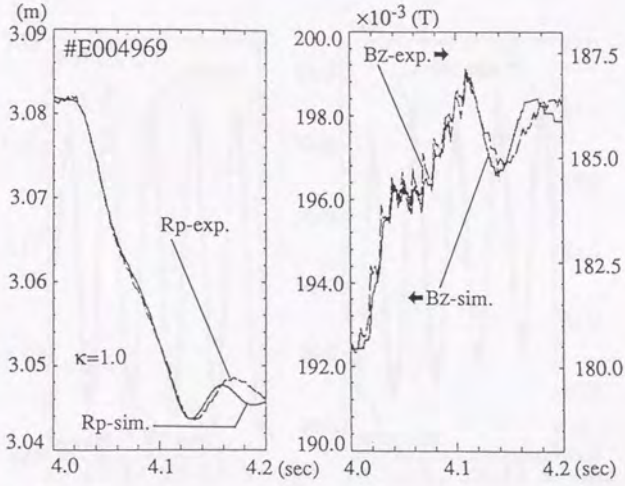

(b) Rp step response

Fig. 3.2 Determination of the Parameters in the ECD model [(a) & (e)] and Comparison between the Experiment and ECD-simulation [(b)~(d), (f)~(h)]. Note: Solid line shows simulation; Broken line shows experiment.

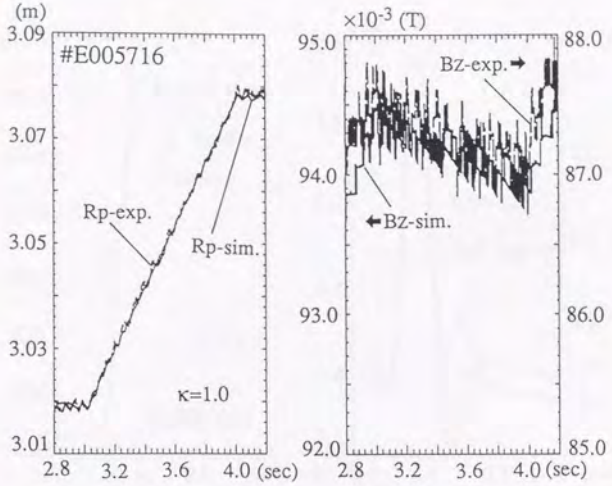

(c) Rp outward displacement

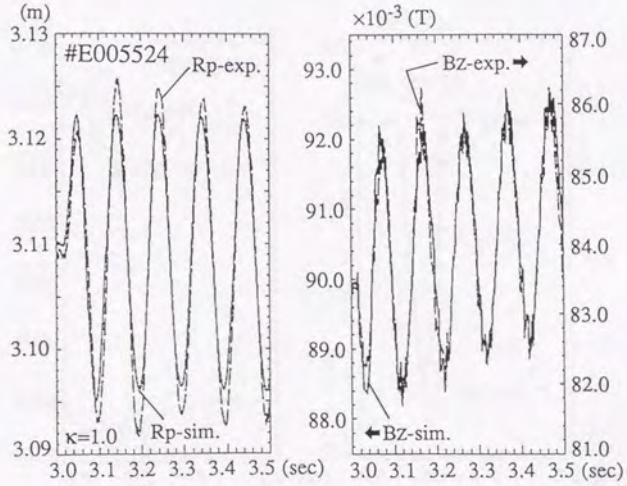

(d) Rp oscillation experiment with a frequency of 10 Hz

Fig. 3.2 Determination of the Parameters in the ECD model [(a) & (e)] and Comparison between the Experiment and ECD-simulation [(b)~(d), (f)~(h)].
Note: Solid line shows simulation; Broken line shows experiment.

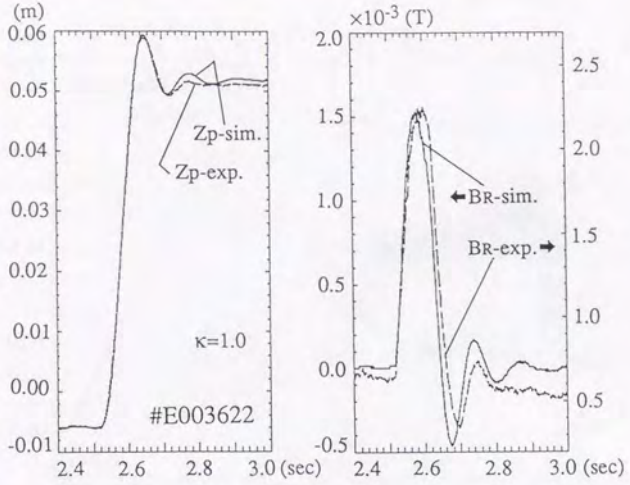

(e) Zp upward step response

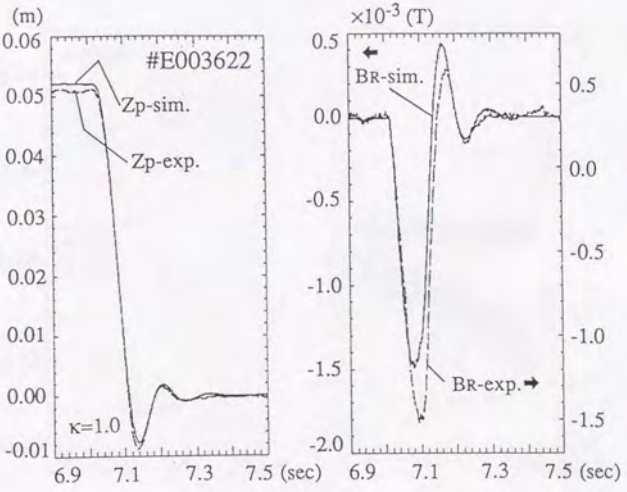

(f) Zp downward step response

Fig. 3.2 Determination of the Parameters in the ECD model [(a) & (e)] and Comparison between the Experiment and ECD-simulation [(b)~(d), (f)~(h)].
Note: Solid line shows simulation; Broken line shows experiment.

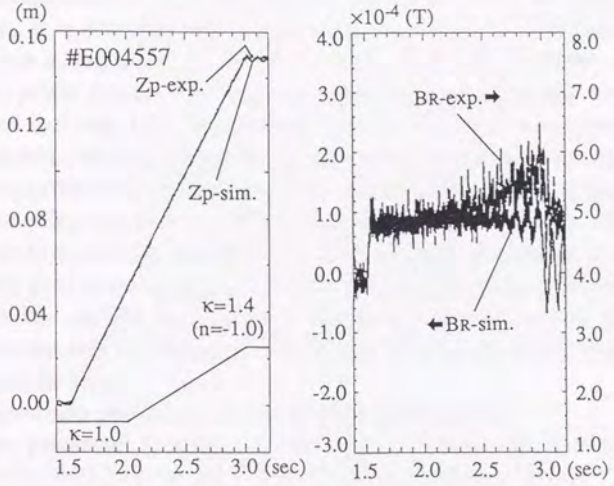

(g) Zp upward displacement with κ change (1.0→1.4)

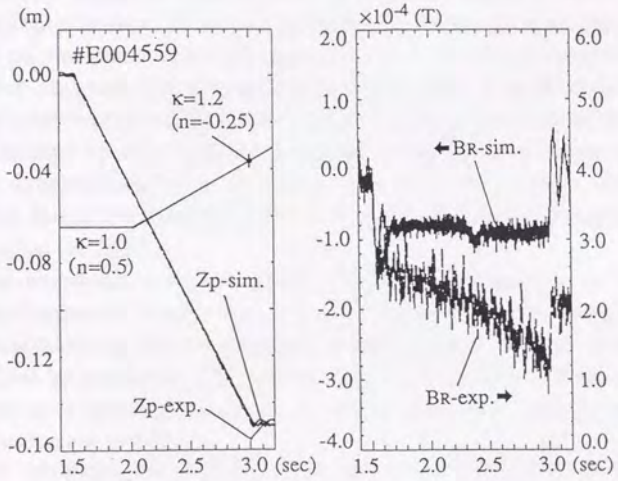

(h) Zp downward displacement with κ change (1.0→1.2)

Fig. 3.2 Determination of the Parameters in the ECD model [(a) & (e)] and Comparison between the Experiment and ECD-simulation [(b)–(d), (f)–(h)]. Note: Solid line shows simulation; Broken line shows experiment.